Title

Two-dimensional perovskite templates for durable, efficient formamidinium perovskite solar cells

Journal

Science, 384(6701)

ISSN

0036-8075

Authors

Sidhik, Siraj

Metcalf, Isaac

Li, Wenbin

et al.

Publication Date

2024-06-14

DOI

10.1126/science.abq6993

Two-dimensional perovskite templates for durable, efficient formamidinium perovskite solar cells

Siraj Sidhik[1,2#], Isaac Metcalf[1#], Wenbin Li[3], Tim Kodalle[4], Connor Dolan[5], Mohammad Khalili[2], Jin Hou[1], Faiz Mandani[2], Andrew Torma[3], Hao Zhang[3], Rabindranath Garai[2], Jessica Persaud[2], Amanda Marciel[2], Itzel Alejandra Muro Puente[6], G. N. Manjunatha Reddy[6], Adam Balvanz[7], Mohamad A. Alam[8], Claudine Katan[9], Esther Tsai[10], David Ginger[11], David Fenning[5], Mercouri G. Kanatzidis[12], Carolin M. Sutter-Fella[4], Jacky Even[13]* and Aditya D. Mohite[1,2]*

[1]Material Science and Nanoengineering, Rice University, Houston, TX 77005, USA.

[2]Department of Chemical and Biomolecular Engineering, Rice University, Houston, TX 77005, USA.

[3]Applied Physics Graduate Program, Smalley-Curl Institute, Rice University, Houston, TX, 77005, USA.

[4]Molecular Foundry, Lawrence Berkeley National Laboratory, Berkeley, CA 94720, USA

[5]Department of Nanoengineering, University of California, San Diego, La Jolla, CA 92093, USA.

[6]University of Lille, CNRS, Centrale Lille Institut, Univ. Artois, UMR 8181-UCCS-Unité de Catalyse et Chimie du Solide, F-59000 Lille, France

[7]Department of Chemistry, Northwestern University, Evanston, IL 60208, USA.

[8]School of Electrical and Computer Engineering, Purdue University, West Lafayette, IN, USA.

[9]Univ Rennes, ENSCR, CNRS, ISCR-UMR 6226, Rennes F-35000, France.

[10]Center for Functional Nanomaterials, Brookhaven National Laboratory, Upton, NY, USA

[11]Department of Chemistry, University of Washington, Seattle 98195.

[12]Department of Chemistry and Department of Materials Science and Engineering, Northwestern University, Evanston, IL 60208, USA.

[13] Univ Rennes, INSA Rennes, CNRS, Institut FOTON - UMR 6082, Rennes F-35000, France.

***Correspondence to: jacky.even@insa-rennes.fr; adm4@rice.edu**

Abstract

We present a design strategy for fabricating ultra-stable, phase pure films of formamidinium lead iodide ($FAPbI_3$) by lattice templating using specific two-dimensional (2D) perovskites with FA as the cage cation. When a pure $FAPbI_3$ precursor solution is brought in contact with the 2D perovskite, the black phase forms preferentially at 100 °C, much lower than the standard $FAPbI_3$ annealing temperature of 150 °C. X-ray diffraction and optical spectroscopy suggest that the resulting $FAPbI_3$ film compresses slightly to acquire the (011) interplanar distances of the 2D perovskite seed. The 2D templated bulk $FAPbI_3$ films exhibited an efficiency of 24.1% in a p-i-n architecture with 0.5 cm^2 active area, and an exceptional durability with T_{97} of 1000 hours under 85 °C and maximum power point tracking.

Perovskite light absorbers with the chemical formula $APbI_3$ (where A is a monovalent cation) have been extensively studied in photovoltaic devices. Among the commonly used A-site cations, such as formamidinium (FA), methylammonium (MA), and caesium (Cs^+), FA has shown promising performance because of its lower bandgap (E_g), improved optoelectronic properties, and higher thermal stability compared to MA *(1).* The larger size of the FA cation yields the Pm3m cubic perovskite lattice through close packing, rather than the lower-symmetry tetragonal (I4/mcm) lattice of $MAPbI_3$ *(2,3).* The lower E_g value of $FAPbI_3$ results from a high degree of Pb 6s - I 5p orbital overlap and reduction of octahedral tilts. The $FAPbI_3$ lattice appears to be a polymorphous network where the average high symmetry structure results from a random distribution of local lower-symmetry (distorted) structural motifs *(4)*. The complexity of the α- (black) phase of 3D bulk $FAPbI_3$ is also reflected by the distribution of the reported average lattice parameter values ranging at room temperature (RT) from *a* ranging from 6.352 to 6.365 Å *(5,6)*.

Moreover, the high symmetry of the $FAPbI_3$ lattice comes at the expense of phase stability. The Goldschmidt tolerance factor of the black α-phase of three-dimensional (3D) $FAPbI_3$ (0.987) is at the edge of the stable range for the perovskite structure (0.8 to 1.0) because the FA cation is almost too large for the A-site *(7)*. As a result, the room temperature (RT) strain-free α-phase of $FAPbI_3$ presents vanishing shear and bulk elastic moduli, and a metastability against the reconstructive phase conversion to the yellow, photoinactive non perovskite δ-phase *(5,8)*. Alloying FA with Cs, MA, or both at the A-site can reduce the effective A-site radius of the perovskite structure and lower the tolerance factor, which improves phase stability at RT but comes at the expense of a widened bandgap *(9-11)*.

Kinetically trapping the α-phase of $FAPbI_3$ is one of the key steps to achieve stable solar cell operation at RT *(12)*. Recently, there have been several reports on FA-based perovskites which with certified power conversion efficiencies (PCEs) exceeding 25% (record 26.2%) for n-i-p *(13-20),* and 24% for p-i-n device architectures *(21-24)*, often by incorporating high concentrations of methylammonium chloride (MACl) *(25)*, formamidinium formate *(16)*, methylene diammonium dichloride *(26),* isopropyl ammonium chloride *(27)*, and methylammonium formate *(28)*, to stabilize the black phase with a E_g of 1.52 eV or higher. The large E_g (compared to the lowest-reported $FAPbI_3$ value of 1.45 eV obtained on single crystals *(5,29)*) is indicative of alloying between FA and MA at the A-site of the perovskite lattices. Other cations, such as Cs^+ *(9,30)*, and Rb^+ *(20,31)*, have also been studied for their potential to improve stability.

Nonetheless, the stability of these FA-based solar cells is still limited, specifically under temperatures exceeding 60°C and AM1.5G light illumination under operation at maximum-power-point tracking (MPPT). Recently, multiple studies have used bulky amine salts with $FAPbI_3$ to stabilize the α-phase through the formation of a metastable two-dimensional (2D) perovskite phase

(19,27,32-40). These 2D perovskites have the chemical formula $A'_2A_{n-1}Pb_nI_{3n+1}$, where A' is a bulky monoammonium cation and n controls the thickness of the perovskite layers. Inspired by this success, we opted to combine in-plane lattice matched 2D perovskites with $FAPbI_3$, to create lattice-matched interfaces using our newly introduced 2D memory seeds method, instead of employing amine salts *(41-43)*.

Here, we show that bulk $FAPbI_3$ forms a highly stable black phase at a temperature well below the δ-$FAPbI_3$ to α-$FAPbI_3$ transition temperature by templating the (001) interplanar spacing of 3D $FAPbI_3$ to the (011) interplanar spacing of a judiciously selected 2D phase (the respective Pb-Pb interatomic spacing for each structure). The $FAPbI_3$ precursors, when drop-cast over a film of Ruddlesden-Popper (RP) phase 2D perovskite $A'_2FAPb_2I_7$, where the A' cation can be butylammonium (BA), or pentylammonium (PA), converted into black phase $FAPbI_3$ at temperatures as low as 100 °C, which is well below the 150 °C temperature at which additive-free control films underwent a yellow-to-black phase transition.

From our studies of film formation using correlated wide-angle x-ray scattering (WAXS), optical absorbance, and photoluminescence (PL), we hypothesized that the resulting black $FAPbI_3$ phase exhibited a lattice constant corresponding to the $d_{(011)}$ interplanar spacing of the underlying 2D perovskite. We could also translate the 2D-templated stabilization of $FAPbI_3$ to scalable solution-processed methods by adding the pre-synthesized 2D perovskites powders (0.5-1.0 mol%) into the $FAPbI_3$ precursor solutions. In a heterophase 3D-2D FA-based film, the phase-stable 2D perovskite nucleated first because had a lower enthalpy of formation and was the phase stable at RT. The 2D structure presented a perovskite surface on which the 3D perovskite can form by distorting to adopt the underlying 2D lattice periodicity, allowing for the preferential templating of the 3D perovskite on the 2D phase during subsequent film annealing. The obtained

bulk films of $FAPbI_3$ exhibit a bandgap (E_g) of 1.48 eV and demonstrate exceptional durability under aggressive ISOS-L-2 conditions of 85ºC/AM1.5G illumination and a PCE of 24.1% in a p-i-n device architecture on a 0.5 cm^2 device area. We believe that these results validate a novel design strategy for the templated growth of 3D perovskites using designer 2D perovskites, which share a nearly identical lattice constant.

Black phase stabilization of $FAPbI_3$ with 2D perovskite template

The general design principle, the selection criteria, and proof-of-concept for the 2D perovskite-based templating of $FAPbI_3$ are shown in **Fig. 1**. **Fig. 1A** shows the in-plane lattice parameter corresponding to the Pb-I-Pb distance, along directions perpendicular to the (011) plane for the 2D $BA_2FAPb_2I_7$ perovskite and the (001) plane for the 3D $FAPbI_3$ perovskite, as a function of layer thickness (n-value) for 2D perovskites formed with a variety of A' site cations. The grey horizontal bar represents the range of reported lattice parameters for bulk $FAPbI_3$ taken single-crystal structural studies *(5,6)*. The $(011)^{2D}$ interplanar spacings were calculated from crystal structures obtained with single-crystal diffraction of each 2D perovskite. Based on the lattice parameters, we hypothesized that the lattice mismatch between the 2D and 3D perovskites must be kept low to minimize the 2D-3D interfacial energy and encourage growth through templating.

We searched for FA-based 2D perovskites with an in-plane lattice parameter close to $FAPbI_3$. As a result, we identified that 2D n=2 FA-based perovskites with the bulky cations butylammonium (BA) and pentylammonium (PA), with lattice constants of 6.359 Å and 6.364 Å respectively, were almost perfectly lattice matched with that of 3D $FAPbI_3$ lattice parameters. However, our crystal structure analysis revealed that the phenylethylammonium (PEA) and octylammonium (OA) n=2 Pb-I-Pb distance was too small (6.265 Å and 6.336 Å, lattice mismatch of 1.5% and 0.5%, respectively) to match the 3D $FAPbI_3$ structure. Notably, all the n=1 2D

perovskites considered were lattice mismatched with $FAPbI_3$ and were not viable options for templating the 3D phase.

Fig. 1B illustrates the crystal structure of α-$FAPbI_3$ and $BA_2FAPb_2I_7$ (BA n=2) 2D perovskite, with a focus on the (001) and (011) planes. The typical 2D perovskite structure of $BA_2FAPb_2I_7$ is shown, displaying the in-plane (001) and (011), and out-of-plane (200) lattice planes. **Fig. 1C** to **1F,** describes a preliminary experiment on the growth of a layer of $FAPbI_3$ on a crystal of $BA_2FAPb_2I_7$. **Fig. 1C** (schematic) and **Fig. 1D** (optical images) shows the experiment at different stages in time. We first partially covered a substrate with a film of red coloured, millimeter-scale $BA_2FAPb_2I_7$ monocrystals that were fabricated with the air-liquid interface method and spread on an indium tin oxide (ITO) glass substrate. Once these crystals were dried on a hotplate at 100°C, we wiped away half the glass slide to create a bare glass region on about half of the glass area. We then added a few drops of $FAPbI_3$ precursor solution (composed of an equimolar ratio of FAI and PbI_2) onto the blank surface and annealed the substrate at a temperature of 100°, 125°, or 150°C (experiments shown in **Fig. 1** were performed at a substrate temperature of 100°C). The solution flowed over and react with the $BA_2FAPb_2I_7$ 2D perovskite crystal film. Upon contact with the 2D crystals, the solution spontaneously (within 10 to 15 s) transformed into a shiny black film. The same transformation was obtained for annealing temperatures of 125° and 150°C. After letting the film equilibrate for 5 min, we obtained three distinct regions on the substrate (**Fig. 1D)**.

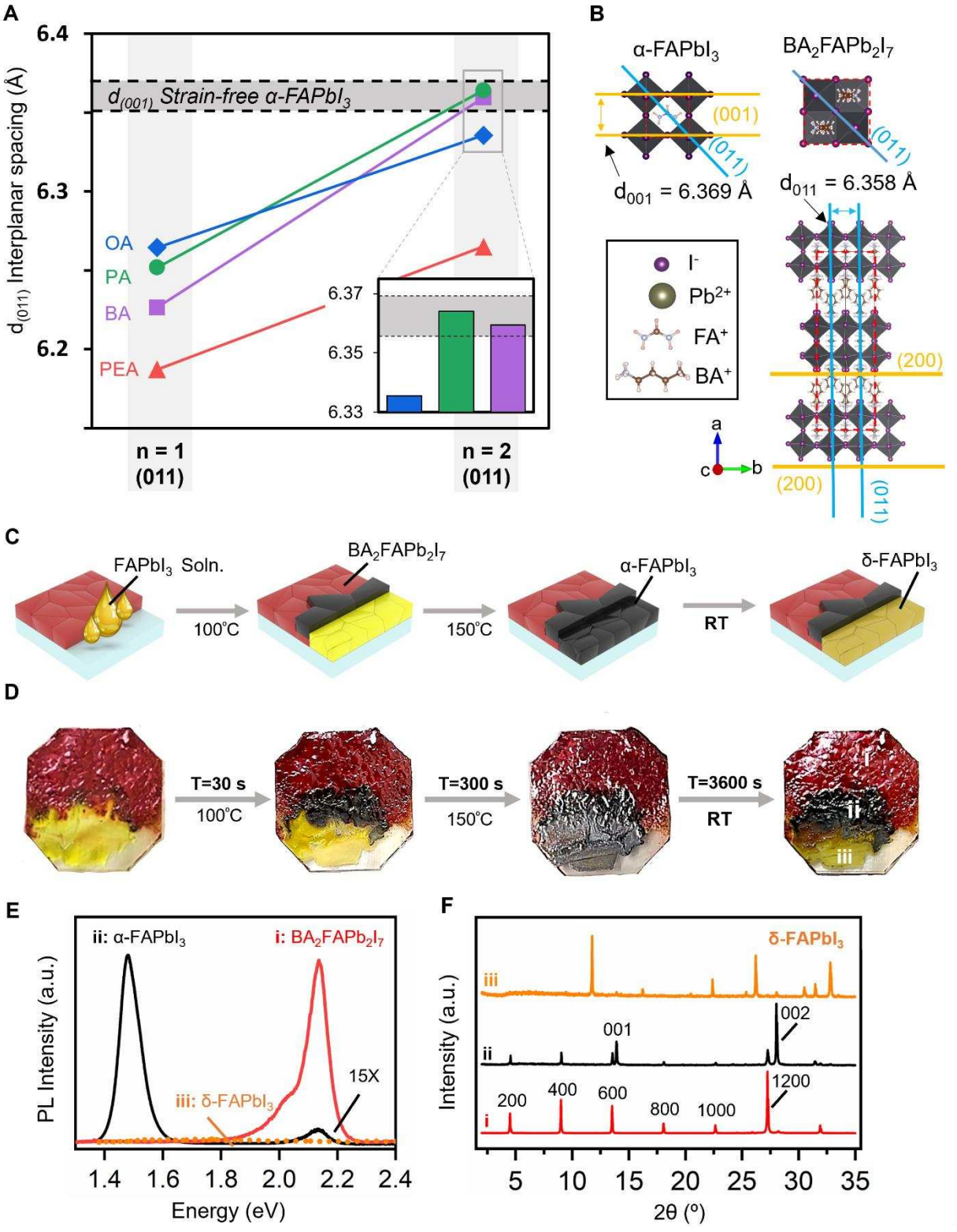

Fig. 1. Design principle and proof-of-concept for 2D perovskite lattice templating of $FAPbI_3$. **A)** The $d_{(011)}$ interplanar spacing for n=1 and FA-based n=2 2D perovskites with various A' cations: PA, BA, OA, and PEA. The range of reported values for $FAPbI_3$ $d_{(001)}$ interplanar spacing

is plotted as gray horizontal bar. Both $BA_2FAPb_2I_7$ and $PA_2FAPb_2I_7$ exhibit a $d_{(011)}$ nearly identical to the $d_{(001)}$ of $FAPbI_3$, as shown in the inset. **B)** Diagram of the unit cells of $FAPbI_3$ (left) and $BA_2FAPb_2I_7$ (right). The (001) and (011) planes are drawn for each structure. The Pb-I-Pb distance corresponds to the (001) interplanar spacing of $FAPbI_3$ and to the (011) spacing of $BA_2FAPb_2I_7$. **C**) Schematics of the templated $FAPbI_3$ drop-coating experiment. First $FAPbI_3$ precursor solution was dropped onto a glass substrate and allowed to flow over crystals of $BA_2FAPb_2I_7$. When heated, the δ-$FAPbI_3$ on top of the $BA_2FAPb_2I_7$ transformed to α-$FAPbI_3$ before the δ-$FAPbI_3$ on top of the bare substrate. Left in ambient air, the α-$FAPbI_3$ on top of the bare substrate transformed to δ-$FAPbI_3$ before the α-$FAPbI_3$ on top of the $BA_2FAPb_2I_7$. **D)** Corresponding photographs of the experiment in **(C)** showing the three distinct regions of the substrate. i: $BA_2FAPb_2I_7$ without $FAPbI_3$ solution, ii: $BA_2FAPb_2I_7$ below $FAPbI_3$ solution, and iii: $FAPbI_3$ solution on bare glass. **E)** PL, and **(F)** XRD of regions i, ii, and iii after 1 hour of exposure to ambient air, showing that the α-$FAPbI_3$ was stabilized when deposited above $BA_2FAPb_2I_7$.

The lower region of the substrate, which was originally bare, changed to a black color with partially converted α-$FAPbI_3$, at 100 °C. The middle region where the solution touched the 2D perovskite consisted of the black phase $FAPbI_3$ on the surface and $BA_2FAPb_2I_7$ below that. Finally, the top part of the substrate where the solvent did not flow remained as $BA_2FAPb_2I_7$ of millimeter-sized monocrystal film. We then left the film for 1 hour under ambient conditions. As the temperature decreased, the bottom region (originally the bare glass region) converted to the yellow phase of $FAPbI_3$ while the intermediate region remained black, suggesting the successful phase stabilization of the $FAPbI_3$. The $BA_2FAPb_2I_7$ crystal film remained unchanged over this time because of its inherent stability compared to its 3D counterpart.

We characterized the three regions of the final film using both PL and XRD measurements. **Fig. 1C** shows the PL spectra of the film obtained at the three specific regions, labelled (i), (ii), and (iii). The dominant PL of region (i) at 2.15 eV corresponded to the ground-state excitonic emission of $BA_2FAPb_2I_7$ film, accompanied by a small shoulder around 2.0 eV. The intermediate region (ii) showed strong emission at 1.48 eV corresponding to the intrinsic bandgap of the α-$FAPbI_3$ phase, with very weak emission at around 2.15 eV from $BA_2FAPb_2I_7$. These results indicated the coexistence of the bulk black phase $FAPbI_3$ 3D perovskite atop the 2D perovskite

crystal film. The presence of the 2D perovskite at the bottom was confirmed by PL measurements taken from the back of the film in region (ii), which exhibited emission solely from the 2D perovskite. As anticipated, no emission was observed from region (iii) that contained the photoinactive yellow phase of the $FAPbI_3$. Additional PL analysis for the drop-coating experiment is shown in **Fig. S1**. The detection of n=3 ($BA_2FA_2Pb_3I_{10}$) in the photoluminescence (PL) measurement acquired from the rear side provides clear evidence of the intercalation process, a phenomenon previously reported by our group (refer to **Fig. S1**) (*44*). We emphasize that the phase stabilization of $FAPbI_3$ occurred also at 100° and 125°C, which are well below the standard annealing temperatures of 150° to 160°C.

The XRD measurements presented in **Fig. 1F** validated the findings from the measurements in **Fig. 1, C to E**. Region (i) showed a pure 2D $BA_2FAPb_2I_7$ perovskite as evidenced by the strong interlayer (h00) XRD plane originating from the inorganic layer stacking. From region (ii), we found a similar XRD pattern but with the (001) and (002) diffraction planes from the α-phase $FAPbI_3$ perovskite that indicates the presence of a mixture of 2D and 3D perovskites. In region (iii), XRD showed only the presence of the δ-phase $FAPbI_3$.

The results shown in **Fig. 1** suggest that the incorporation of $BA_2FAPb_2I_7$ into $FAPbI_3$ during film formation could stabilize the perovskite phase through templating between the two structures' Pb-I-Pb interatomic distances. To test this hypothesis in $FAPbI_3$ films, 2D perovskites were added as templating agents to precursor solutions of 1:1 FAI: PbI_2 in mixed 4:1 DMF: DMSO solvent. We compared the effect of 2D perovskites with four different A'-site cations: BA, PA, OA, and PEA. Using a technique previously developed by our group *(41)*, pre-synthesized 2D crystals were added instead of the more conventional choice of A' cation halide salts. Rather than dissolving completely into constituent ions, 2D crystals in a DMF: DMSO solvent formed sub-

micrometer sized crystallites (termed as memory seeds) that preserved their perovskite structure and served as nucleation sites during film formation. These memory seeds could transfer their initial n-value to solution-processed films. However, when dissolved in a $FAPbI_3$ precursor solution rather than pure DMF: DMSO, 2D perovskite crystallites were surrounded by a high concentration of mobile A-site cations, which tended to intercalate into the seeds and increase their n-value. As a result, a 2D additive with a given A'-site cation will grow from a $FAPbI_3$ solution at its thermodynamically preferred n-value in such an environment. With this in mind, only 2D perovskites of the n-value that will precipitate from a $FAPbI_3$ solution were considered as candidates for α-phase stabilization. Through solution processing experiments summarized in **Fig. S2**, we found that each of the four RP 2D perovskites considered here grew in their n=2 phase from $FAPbI_3$ solution.

Crystallization dynamics of 2D templated $FAPbI_3$ thin films

We used our selectively designed 2D perovskites $BA_2FAPb_2I_7$ and $PA_2FAPb_2I_7$ to grow stabilized $FAPbI_3$ perovskite thin films. **Fig. 2A** visually illustrates the film formation process of $FAPbI_3$ with 2D perovskite additive, offering insight into the visible alterations that occur during the process. Perovskite films were synthesized by spin-coating with precursors of FAI: PbI_2:2D perovskite with a molar ratio of 1:1:x mol%. After antisolvent washing with diethyl ether, the thin film underwent a series of intermediate stages, which can be seen visually as changes in colour from pale red (before annealing) to dark brown, and finally to a black film when annealed at temperatures ranging from 100° to 150°C for 20 minutes.

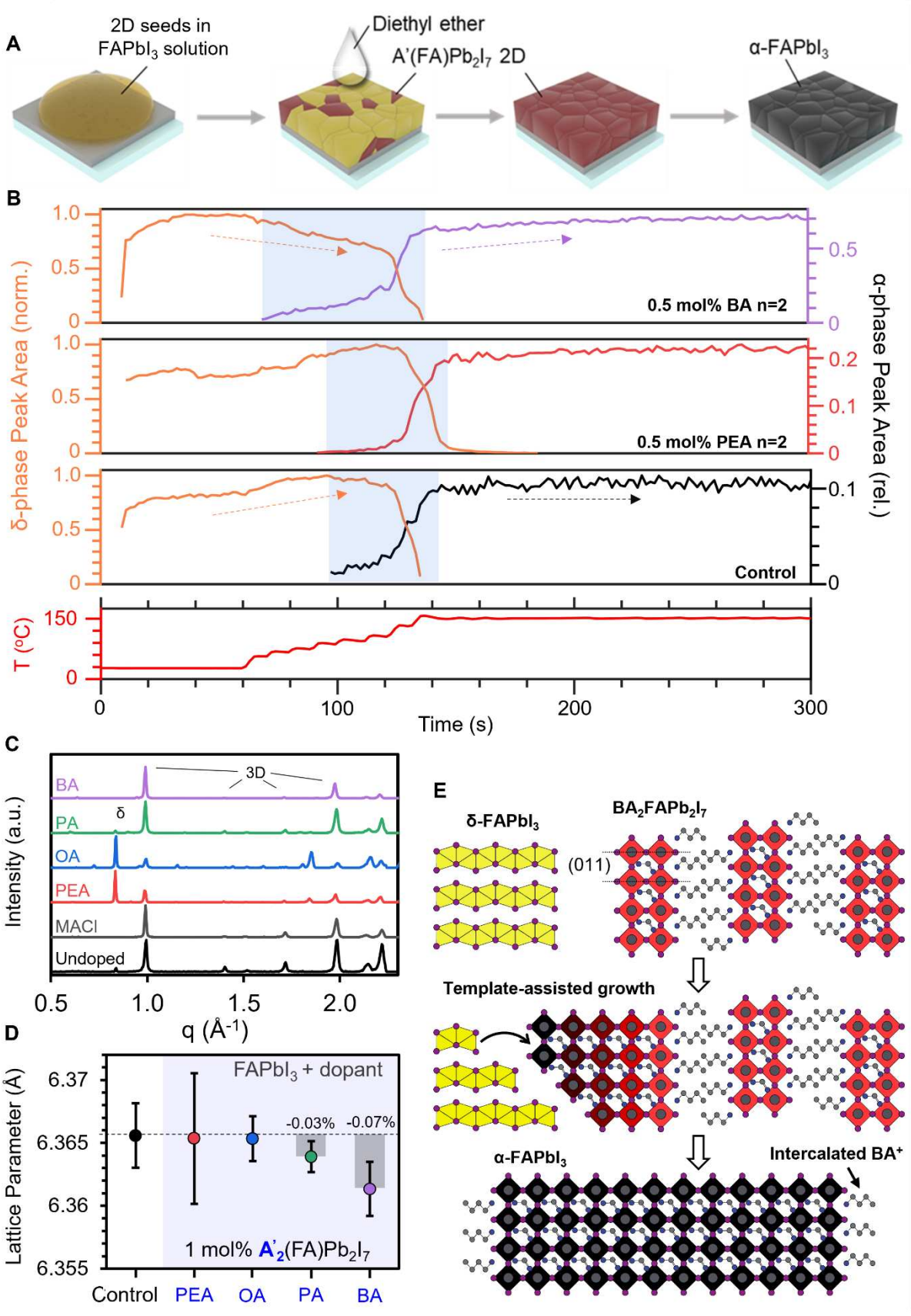
A
2D seeds in
FAPbI3 solution
Diethyl ether
A'(FA)Pb2I7 2D
α-FAPbI3
B
δ-phase Peak Area (norm.)
α-phase Peak Area (rel.)
0.5 mol% BA n=2
0.5 mol% PEA n=2
Control
T (°C)
Time (s)
C
Intensity (a.u.)
BA
PA
OA
PEA
MACl
Undoped
3D
δ
q (Å-1)
D
Lattice Parameter (Å)
FAPbI3 + dopant
-0.03%
-0.07%
1 mol% A'2(FA)Pb2I7
Control
PEA
OA
PA
BA
E
δ-FAPbI3
BA2FAPb2I7
(011)
Template-assisted growth
α-FAPbI3
Intercalated BA+

222

Fig. 2. 2D-stabilized $FAPbI_3$ film formation mechanism. A) Fabrication steps of a 2D crystal templated $FAPbI_3$ thin film, **B)** Integrated peak areas for the $(100)^{\delta}$ (orange, left axis) and $(001)^{3D}$ (black, right axis) peaks over time for control $FAPbI_3$ (bottom), $FAPbI_3$ with 0.5 mol% PEA n=2 added (middle), and $FAPbI_3$ with 0.5 mol% BA n=2 added (top). The $(001)^{3D}$ peak area as indicated on the right vertical axis is normalized to the maximum of the $(100)^{\delta}$ peak area. The regions between the emergence of the $(001)^{3D}$ peak and the full conversion to α-$FAPbI_3$ are highlighted in blue. **C)** Azimuthally integrated WAXS patterns averaged across the first 90 seconds of annealing after reaching 150ºC for each $FAPbI_3$ additive tested (2D concentration is 1 mol%). **D)** The α-$FAPbI_3$ (001) lattice parameter for films with 1 mol% of each 2D additive, as measured on separately fabricated samples at RT. Error bars indicate standard deviation based on data from 3 to 5 samples. **E)** Schematic diagram illustrating the mechanism of lattice-matched 2D templated $FAPbI_3$ perovskite formation.

To elucidate the mechanism that produces a RT phase-stable $FAPbI_3$ film, we measured the structural dynamics of the perovskite during thin-film formation using synchrotron-based WAXS. The perovskite thin-films were deposited from solution onto a bare ITO substrate by using a robotic antisolvent pipette and a resistive-heating spin-coater in a WAXS chamber under a nitrogen atmosphere (**Fig. S3**). We first investigated the crystallization kinetics of a $FAPbI_3$ film with 1 mol% $BA_2FAPb_2I_7$ incorporated. A WAXS pattern taken during thin-film formation (**Fig. S4)** showed concentric diffraction rings corresponding to the Bragg reflections of the stacking axis diffraction planes of $BA_2FAPb_2I_7$ and α- and δ- phases of 3D-$FAPbI_3$. The diffraction peaks correspond to crystallographic planes in the 2D, α-$FAPbI_3$, and δ-$FAPbI_3$ crystal structures.

The WAXS pattern was azimuthally integrated and plotted as a function of time along with spin speed and temperature to observe the film's structural evolution (**Fig. S4**). In this in-situ experiment can be divided into four stages: (i) antisolvent dropping during spin-coating; (ii) after spin-coating but before annealing; (iii) slow annealing ramping from RT to 150°C; and (iv) constant annealing at 150°C. The δ- phase $FAPbI_3$ immediately formed after depositing antisolvent (10 s), as indicated by the strong $(100)^{\delta}$ (q, the length of the reciprocal lattice vector, is 0.84 $Å^{-1}$), $(101)^{\delta}$, and $(110)^{\delta}$ diffraction planes (drawn in **Fig. S5**). Once the spin-coating is completed (30 s),

the δ-phase persisted as 2D $BA_2FAPb_2I_7$ seeds began to crystallize at RT, illustrated by the out-of-plane $(400)^{2D}$ ($q = 0.65Å^{-1}$) and $(600)^{2D}$ ($q = 0.96Å^{-1}$) diffraction peaks (**Fig. S4**).

Next, a nonlinear stepwise annealing sequence was applied, in which the substrate temperature was increased by steps of 20°C in 20 second intervals up to 100°C and then increased by steps of 25°C up to 150°C (stage iii). Slow ramping to 150°C allowed us to observe the onset temperature of the $FAPbI_3$ α-phase. In this stage, for annealing at low temperatures (<100°C), the diffraction intensity of the 2D increased and a new peak emerged near $q = 1Å^{-1}$ corresponding to the $(001)^{3D}$ plane from α-phase $FAPbI_3$. **Fig. 2B, top** shows the integrated peak area for the $(100)^{\delta}$ and $(001)^{3D}$ peaks as a function of time for $FAPbI_3$ with 0.5 mol% BA n=2 incorporated. The $(001)^{3D}$ peak emerged after 75 s and slowly increases in intensity as the $(100)^{\delta}$ peak simultaneously decreases. Around after 130 s (T = 130°C), the remaining δ-phase abruptly converted into α-phase. As the film continued to anneal at 150°C for the remainder of the experiment (stage iv), the 2D diffraction peaks slowly faded and the α-phase $FAPbI_3$ peaks slowly grew more intense.

We repeated this experiment for four other types of precursor solutions. For additive-free $FAPbI_3$: **Fig. S6A** shows the in-situ contour WAXS plot for a 1:1 FAI:PbI_2 solution. In contrast to the $FAPbI_3$-2D sample, which exhibited a gradual emergence of α-phase between 100° and 150°C followed by a complete δ → α transformation at 130°C, the additive-free (control) $FAPbI_3$ showed a much more abrupt transition from δ-phase to α-phase near 150°C (**Fig. 2B, bottom**) consistent with previous reports. The $(001)^{3D}$ peak emerged later with a shorter tail in control $FAPbI_3$, and the $(100)^{\delta}$ peak did not prematurely decrease as in the film that incorporated BA n=2 We observed a much lower $(001)^{3D}$ peak intensity (relative to the $(100)^{\delta}$ peak intensity) for control pristine $FAPbI_3$ compared to $FAPbI_3$ with BA n=2 additive, suggesting a lowered crystallinity. Unlike the

film with added BA n=2, the $(001)^{3D}$ peak of control $FAPbI_3$ did not grow more intense as annealing at 150°C continued.

For a precursor solution of 1:1:35 mol% FAI: PbI_2: MACl in 4:1 DMF: DMSO, which is commonly used to grow phase stabilized $FAPbI_3$ *(25)*, the introduction of MA into the A-site of $FAPbI_3$ lowered the effective tolerance factor and stabilized the α-phase at a lower temperature compared to additive-free $FAPbI_3$. As a result, the abrupt $\delta \rightarrow \alpha$ transformation occurred at 75°C for the $FAPbI_3$-MACl sample (**Fig. S6B and S10A)**. However, like the control sample and in contrast to the 2D-templated sample, no region of gradual $\delta \rightarrow \alpha$ transformation was observed.

Next, BA n=2 was added to 1:1 PbI_2: FAI with concentrations of 0.25, 0.5, and 1.0 mol%. **Fig. S7** shows contour plots of the in-situ WAXS experiment for additive concentrations of 0.25 mol% (top) and 1.0 mol% (bottom). In all cases, the incorporation of BA n=2 increased the $(001)^{3D}$ peak intensity relative to the control, suggesting that even minute amounts of BA n=2 could improve α-phase crystallinity. The 0.5 mol% BA n=2 incorporated $FAPbI_3$ showed a similar film formation process to the 1.0 mol% sample discussed above, that is, a decrease in the $(100)^{\delta}$ peak and a slow emergence of the $(001)^{3D}$ peak at a lowered temperature. However, 0.25 mol% BA n=2 incorporation did not lower the onset temperature of the $(001)^{3D}$ peak relative to the control, and did not cause the same characteristic decrease in $(100)^{\delta}$ intensity below 150°C. The phase-stabilization appeared to be concentration invariant down to a certain minimum 2D concentration, below which the templating effect was lost but the film crystallinity was still improved.

We then examined a series of 2D additives including PA n=2, OA n=2, and PEA n=2. We note that the effect PA n=2 was similar to that of BA n=2, lowering the onset temperature of the α-phase peak and causing a decrease in the δ-phase below 150°C (**Fig. S8 and S10B**). In contrast, OA n=2 and PEA n=2 have markedly different effects (**Fig. S9 and S10B)**. For OA n=2, the 2D

peaks formed weakly and the α-phase emerged earlier than for the control sample, but no δ → α transformation was observed. Instead, the δ-phase persisted throughout annealing, suggesting that $OA_2FAPb_2I_7$ seeds could serve as nucleation sites for $FAPbI_3$ to a limited extent but slowed the δ → α transformation. $FAPbI_3$ with 0.5 mol% PEA n=2 additive showed no 2D peaks and no early α-phase emergence (**Fig. 2B, middle**). Moreover, $FAPbI_3$ with 1 mol% PEA n=2 also retained δ-phase peaks throughout the measurement, suggesting that the $PEA_2FAPb_2I_7$ not only failed to form seeds for templating $FAPbI_3$ but also suppressed δ → α transformation kinetics. **Fig. 2C** shows the azimuthally integrated WAXS patterns of $FAPbI_3$ samples with 1 mol% 2D, averaged across the first 90 s of annealing at 150°C. This plot revealed the incomplete δ → α transformation for the films incorporating 1 mol% OA and PEA n=2, contrasting with the complete transformation for 1 mol% BA and PA n=2 (also visible in **Fig. S10**). Interestingly, all 2D films showed a slow decrease in the 2D peak intensities and a slow increase in the $(001)^{3D}$ peak intensity during annealing at 150°C that was not observed for the control film (**Fig. 2B and Fig. S10**). Although gradual volatilization of the A' cation in $A'_2FAPb_2I_7$, leaving behind $FAPbI_3$ could account for these changes, as discussed below, optical and nuclear magnetic resonance (NMR) results suggest that the 2D phase was not completely lost to volatilization, and that there may be a competing mechanism of 2D restructuring within the lattice.

The in-situ WAXS results suggested that $BA_2FAPb_2I_7$ and $PA_2FAPb_2I_7$ could template α-phase $FAPbI_3$, but $OA_2FAPb_2I_7$ and $PEA_2FAPb_2I_7$ could not. Ex-situ 1D XRD was performed on separate 1 mol% 2D-incorporated $FAPbI_3$ films (**Fig. 2D**) and showed that $FAPbI_3$ films with added OA n=2 or PEA n=2 had an identical $(001)^{3D}$ interplanar spacing as control $FAPbI_3$, but that PA n=2 and BA n=2 caused a small but noticeable compression of the $(001)^{3D}$ interplanar spacing by -0.03% and -0.07%, respectively. Because the $(011)^{2D}$ interplanar spacing was lightly smaller

for BA n=2 than for PA n=2 (**Fig. 1A)**, a higher compressive strain for $FAPbI_3$ with added BA n=2 compared to PA n=2 also supports the (011) lattice templating hypothesis.

To verify our structural results, we performed similar in-situ optical spectroscopy measurements on the $BA_2FAPb_2I_7$-templated $FAPbI_3$ samples. During the initial stages of annealing, the film exhibited a strong excitonic absorption peak at 2.15 eV corresponding to $BA_2FAPb_2I_7$, which with progressive annealing transformed into α-$FAPbI_3$, characterized by a 3D perovskite absorption band edge (**Fig. S11**). Similarly, a strong emission of the $BA_2FAPb_2I_7$ perovskite was observed at 2.15 eV in the in-situ PL measurement, accompanied by a broad emission at lower energies (**Fig. S12**). We hypothesized that the lower energy emissions were from a combination of effects, including edge state emission *(45, 46)*, the formation of higher n-value 2D phases (e.g. n=3 $BA_2FA_2Pb_3I_{10}$) *(47,48)*, and quantum confinement effects of the 2D and $FAPbI_3$ crystallites *(49-52)*. Sub-bandgap edge state emission in $BA_2FAPb_2I_7$ was verified by spatially resolved PL, which showed a 1.8 eV PL emission peak only at the edges of an exfoliated $BA_2FAPb_2I_7$ single crystal. Additionally, the presence of a PL emission peak at 1.85eV and the observation of n=3 excitons in power-dependent PL indicate that FA intercalation increases the layer thickness from n=2 to n=3 during annealing. A similar broad emission below the n=2 bandgap was observed during film formation for $FAPbI_3$ with $PA_2FAPb_2I_7$ additive **(Fig. S12)**, consistent with the structural results for $PA_2FAPb_2I_7$ shown in **Fig. S8**. However, no sub-bandgap emission was observed for the control $FAPbI_3$ or for $FAPbI_3$ incorporating MACl, $OA_2FAPb_2I_7$, or $PEA_2FAPb_2I_7$ (**Fig. S13**).

Based on the in-situ WAXS and PL measurements in **Fig. 2** and **Fig. S2 to S10**, we propose the following film formation process mediated by 2D templating. The film first forms grains of *δ*-phase $FAPbI_3$ and 2D seeds at RT. The 2D likely formed initially because of its more negative

formation enthalpy, its RT phase-stability, and the presence of 2D seeds in the precursor solution as confirmed through dynamic light scattering (DLS) measurements shown in **Fig. S14**. During annealing, the δ-phase restructured itself beginning at the low-energy surfaces of the 2D seed crystals to form α-phase $FAPbI_3$. At the interface with $FAPbI_3$, the arrangement of PbI_6 octahedra in a 2D perovskite may facilitate nucleation of a stable α-phase $FAPbI_3$, with subsequent phase transformation toward the bulk *(53)*. Indeed, from **Fig. 2D**, we deduced that the growth mechanism favoured the formation of a compressively strained α-phase (001) plane templated by the 2D (011) interplanar spacing. The low-temperature α-phase formation being only observed for films with added PA and BA n=2, and these films being also the only ones to exhibit lattice strain, is strong evidence for a templating effect off the $(011)^{2D}$ spacing.

The (011) interplanar spacings of $BA_2FAPb_2I_7$ (6.359 Å) and $PA_2FAPb_2I_7$ (6.364 Å) are almost perfectly lattice matched with the $(001)^{3D}$ interplanar spacing of $FAPbI_3$, both falling within the range of reported $FAPbI_3$ lattice constants from 6.352 Å to 6.365 Å *(5,6)*, whereas the (011) interplanar spacings of $OA_2FAPb_2I_7$ (6.336 Å) and $PEA_2FAPb_2I_7$ (6.265 Å) were not well matched. This structural difference explains why OA-2D and PEA-2D did not show the same $\delta \rightarrow \alpha$ conversion process as BA-2D and PA-2D. The templating process and the resulting $FAPbI_3$ strain appeared 2D concentration-independent down to some minimum threshold, which for BA 2D perovskites was between 0.25 and 0.5 mol%. As the temperature was raised to 150°C and the sample continued to anneal, we hypothesize that the 2D perovskite simultaneously volatilized its A' cation and underwent a slow FA intercalation process, which increased its n-value.

Other reports have suggested that the A' cation of 2D perovskites incorporated into $FAPbI_3$ volatilized completely during annealing except for a small fraction left at grain boundaries,[19,37,38] which would also explain the disappearance of our 2D signal over time and the slow increase in

366 the $(001)^{3D}$ peak intensity during annealing at 150°C. Solid-state ^{1}H NMR on scraped films of
367 $FAPbI_3$ with added 2D before and after annealing did reveal a partial volatilization of the spacer
368 cation during film formation, but also confirmed appreciable fractions of BA and PA even after
369 annealing at 150°C for 20 min (**Fig. S15** and **S16**). Time-of-flight secondary-ion mass
370 spectrometry (ToF-SIMS) results suggested that the remaining 2D spacer cations were
371 homogenously distributed up to 1 mol% and for higher concentrations, appeared more pronounced
372 toward the film interface with the substrate (**Fig. S17**).

373 The BA and PA cations lead to the formation of a mixed 2D/3D phase that was challenging
374 to characterize with the aforementioned long-range techniques. Instead, we applied high-field (21
375 T) solid-state NMR spectroscopy to resolve the local structures of the organic cations in the mixed
376 phase (**Fig. S16**). The ^{1}H NMR peaks associated with the large (BA and PA) and small (FA)
377 cations were well resolved so the amount of 2D phase present in the templated $FAPbI_3$ materials
378 could be identified and quantified. In addition, the local structures of the mixed phases, elucidated
379 by analysing 2D ^{1}H-^{1}H correlation NMR spectra (**Fig. S16, C to F**), showed the presence of
380 through-space intermolecular interactions between the large cations (BA or PA) in the 2D phase
381 and the small cations (FA) in the 3D $FAPbI_3$ phase. Based on the data presented above, we
382 illustrate a comprehensive schematic diagram capturing the different stages of film formation in a
383 2D templated $FAPbI_3$ (**Fig. 2E and discussion in SI 1.18**).
384
385
386
387

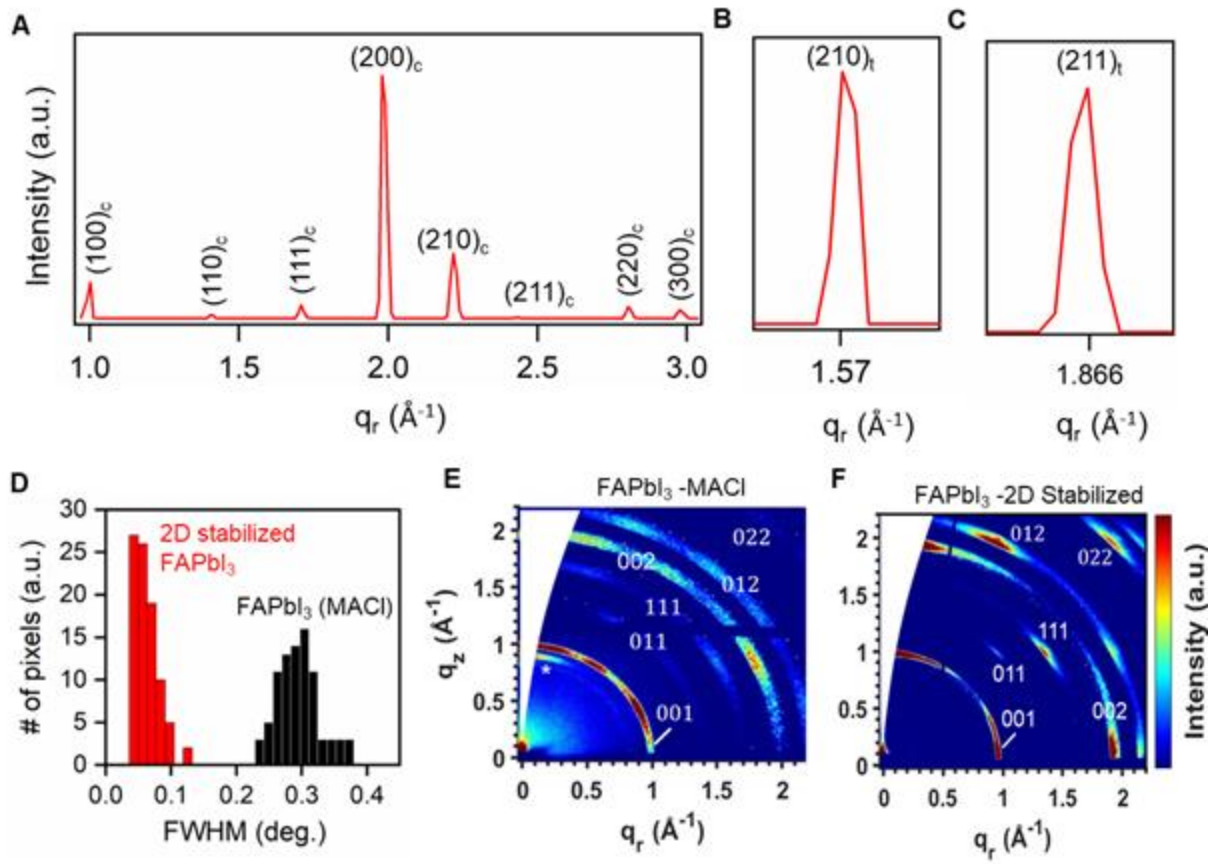

Fig. 3. Ex-situ structural characterization of phase stabilized $FAPbI_3$ films. A) A representative azimuthally integrated nano-XRD pattern for a film of $BA_2FAPb_2I_7$-templated $FAPbI_3$. **B**) The (210), and **C**) the (211) peaks of $BA_2FAPb_2I_7$-templated $FAPbI_3$ which can be seen after integrating several nano-XRD patterns obtained for different pixels within the testing region. These peaks are forbidden in a cubic crystal structure and confirm the existence of tetragonal $FAPbI_3$. **D**) A histogram of nano-XRD peak FWHM values for different pixels of a $BA_2FAPb_2I_7$-stabilized $FAPbI_3$ film (red) and a MACl-stabilized $FAPbI_3$ film (black). 2D-stabilized $FAPbI_3$ shows a significantly lower FWHM. **E** – **F**) Representative GIWAXS patterns for **E**) MACl-stabilized $FAPbI_3$ and **F**) $BA_2FAPb_2I_7$-stabilized $FAPbI_3$.

Structural and optical characteristics of Phase stabilized $FAPbI_3$

We hypothesized that the observed compressive lattice strain applied by the templating 2D phase can result in the formation of a locally segregated tetragonal structure *(54,55)*. To investigate the impact of 2D stabilization on nanoscale structural properties of $FAPbI_3$, we performed nanoscale XRD with a 25-nm spot size x-ray probe on MACl-stabilized $FAPbI_3$ and 2D-stabilized $FAPbI_3$. The high brilliance of a synchrotron light source enabled resolution of diffraction from minority

phases *(56,57)*. As shown in **Fig. S18**, both films showed sufficient x-ray stability to accommodate the measurement. Localized x-ray scattering from both cubic (i.e., α) and tetragonal phases was observed. A representative summed diffraction CCD image from a map of 2D-stabilized $FAPbI_3$ is shown in **Fig. S19**, and an azimuthally integrated pattern is shown in **Fig. 3A**. In addition to intense scattering from the cubic perovskite lattice, we observed two subtle peaks that we indexed to the tetragonal phase, the $(210)_t$ (t=tetragonal) at 1.57 A^{-1} and $(211)_t$ at 1.866 A^{-1} (**Fig. 3, B and C**). The $(211)_t$ peak could not be definitively indexed as tetragonal because of the overlapping $(210)_h$ (h=hexagonal, δ-phase) peak at virtually the same scattering vector, but the $(210)_t$ was unambiguously identified (*58*). Furthermore, because we observed no additional scattering peaks from the hexagonal phase in this sample, we also attribute the $(211)_t$ peak to the tetragonal phase. The diffraction from tetragonal phase was far less intense than diffraction from the cubic phase, with total summed diffraction intensity from the $(211)_t$ peak amounting to 0.8% of the intensity of the (200)c (c=cubic) peak (see **Fig. S19**).

To investigate the impacts of 2D stabilization on the quality of the perovskite crystallites in the thin film, we performed five-dimensional rocking curves (rocking curves with a two-dimensional detector and two-dimensional spatial mapping) on the sample where the angle of the incident x-ray was varied and spatial maps in the plane of the sample were repeated over the same area to precisely analyze the width of the diffraction peak. The 2D-stabilized $FAPbI_3$ exhibited substantially narrower diffraction full-width at half-maximum (FWHM) than the MACl-doped $FAPbI_3$ (**Fig. 3D**). The narrower diffraction peak could be a result of an increase in domain size or reduced microstructural disorder (microstrain) *(59)*. However, the well-established increase in domain size seen when MACl was included in perovskite precursors suggested that a smaller domain size in MACl-doped $FAPbI_3$ was not the cause *(25,60,61)*. We concluded that the 2D-

stabilization resulted in a reduced structural disorder within the crystallites of the thin film, which is consistent with previous reports *(53)*. Halder-Wagner analysis summarized in **Fig. S20** and **S21** further revealed that microstrain in 2D-stabilized $FAPbI_3$ decreased with increasing 2D concentration.

The grazing-incidence WAXS (GIWAXS) patterns of the MACl-doped $FAPbI_3$ perovskite thin films (**Fig. 3E**) and $FAPbI_3$ with $BA_2FAPb_2I_7$ additive revealed two different characteristics of the thin films. The MACl-doped $FAPbI_3$ films exhibited Bragg intensities extended along arc segments, indicating a random orientation of crystal domains or grains within a polycrystalline film (high mosaicity). Furthermore, these films showed PbI_2 diffraction peaks. In contrast, the 2D-stabilized $FAPbI_3$ films reveal well-defined Bragg diffraction spots along the (001) plane, observed along the Debye–Scherrer ring near $q = 1$ Å^{-1}. This distinct observation implied smaller mosaicity and improved grain orientation in the out-of-plane direction, perpendicular to the substrate. Furthermore, mosaicity appeared to be reduced with increasing 2D concentration (**Fig. S22)**. Atomic force microscopy (AFM) likewise showed an increase in $FAPbI_3$ grain size when 2D concentration was increased from 0.25 mol% to 0.5 mol%, although a further increase caused the grain size to decrease (**Fig. S23)**. These results were consistent with the observation in **Fig. S7** of improved crystallinity for $FAPbI_3$ films incorporating even small amounts of BA n=2.

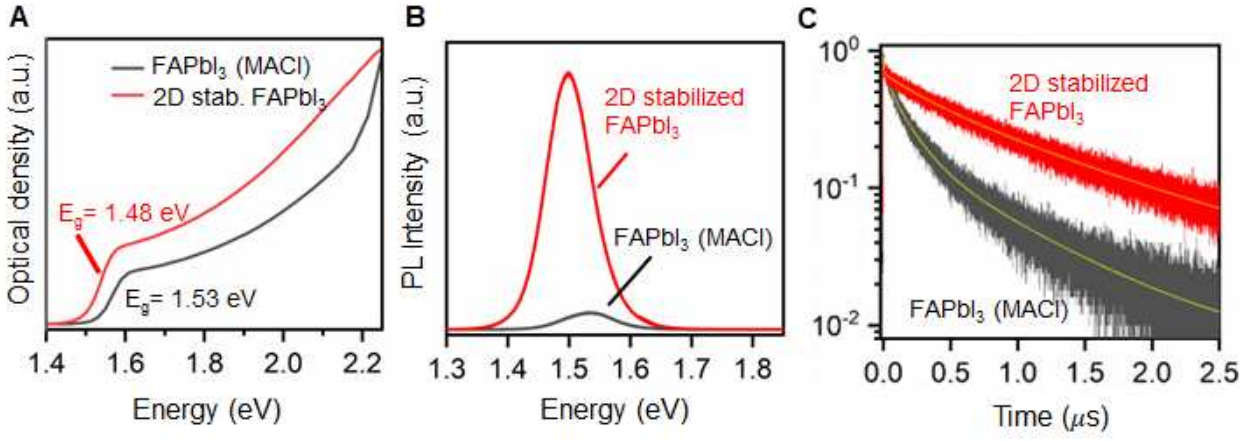

Fig. 4. Optical characterization of the phase stabilized $FAPbI_3$ films. A) Absorption spectra of MACl-stabilized $FAPbI_3$ (grey) and $BA_2FAPb_2I_7$-stabilized $FAPbI_3$ (red) with their band gaps indicated. **B**) PL spectra of MACl-stabilized $FAPbI_3$ (gray) and $BA_2FAPb_2I_7$-stabilized $FAPbI_3$ (red). **C**) TRPL spectra of MACl-stabilized $FAPbI_3$ (gray) and $BA_2FAPb_2I_7$-stabilized $FAPbI_3$ (red).

We observed an increase in the absorption of the 2D stabilized $FAPbI_3$ compared to the MACl-doped $FAPbI_3$. (**Fig. 4A**). Using the Tauc plot calculated from the absorption spectrum (**Fig. S24**), we derived a bandgap of 1.48 eV for the 2D stabilized $FAPbI_3$ (versus the 1.52 eV band gap of the MACl-doped films) that was much closer to the smallest reported (1.45 eV) bandgap of $FAPbI_3$ *(5)*. This band gap reduction (**Fig. 4A-B**) was consistent with experimental signatures pointing toward a reduction of the lattice disorder (**Fig. 3E-F**) *(53)*. In a polymorphous picture of the cubic phase of $FAPbI_3$, the reduction of polymorphism also leads to reduced tilt amplitudes *(4,62)*. As 2D concentration increased, the valence band maximum (VBM) was lowered (**Fig. S25)** and the band gap widened.

We also observed an order of magnitude increase in the PL intensity of the 2D-stabilized $FAPbI_3$ compared to the MACl-doped $FAPbI_3$ indicating reduced nonradiative recombination (**Fig. 4B**). The PL peak positions aligned with the absorption thresholds for both the films. In time-resolved PL measurements (**Fig. 4C**), the 2D stabilized $FAPbI_3$ film exhibited a slower PL decay rate compared to the reference, implying a decrease in nonradiative recombination attributable to a reduction in trap-mediated bulk or surface recombination processes.

Photovoltaic studies

We used 2D stabilized $FAPbI_3$ to fabricate perovskite solar cells using an inverted architecture with MeO-2PACz as the hole transport layer and C_{60} as the electron transport layer. To construct a band diagram of the device architecture (**Fig. 5A**), we measured the valence band maxima and conduction band minima of the MACl-doped $FAPbI_3$ and 2D stabilized $FAPbI_3$ by combining photoemission yield spectroscopy (PES) and absorption measurements. The details of the

measurements are discussed in the methods section of the SI. The 2D stabilized $FAPbI_3$ although slightly shifted toward higher energy compared to the MACl-doped $FAPbI_3$ had an appropriate band alignment for charge carrier separation and extraction.

The current density-voltage (*J–V*) characteristics of the best-performing 2D stabilized $FAPbI_3$ device in reverse and forward bias sweeps are illustrated in **Fig. 5B**. We achieved a power conversion efficiency (PCE) of 24.1% for an active area of 0.5 cm^2 under AM1.5G illumination (**Fig. 5E**) with a short circuit current density (J_{SC}) of 25.5 $mA.cm^{-2}$, open circuit voltage (V_{OC}) of 1.12 V, and fill factor of 82%. These metrics compare favourably with the corresponding thermodynamic limits of 31.1 $mA{\cdot}cm^{-2}$, 1.21 V, and 89%, respectively *(63)*. **Fig. 5C** shows the external quantum efficiency (EQE) for the same device as that of the *J–V* curve. Solar cells under identical conditions using different 2D perovskite concentration were fabricated to confirm the impact of concentration on performance. The statistical distributions of J_{SC}, V_{OC}, fill factor (FF), and PCE for 40 devices of each condition are shown in **Fig. S26**. The J_{SC} obtained by integrating the EQE over the wavelength is 24.3 mA cm^{-2}, which was in good agreement with that of the device's *J–V* curve measured using a solar simulator. For comparison, we fabricated $FAPbI_3$ devices stabilized using $PA_2FAPb_2I_7$, $OA_2FAPb_2I_7$ and $PEA_2FAPb_2I_7$ (see **Fig. S27)**. The PA-templated $FAPbI_3$ device exhibited a PCE of 21%, with a Jsc of 25.2 mA.cm-2, V_{OC} of 1.06V, and FF of 78.1%. In the case of optimized OA- and PEA-templated $FAPbI_3$, we achieved PCEs of 16.54% (J_{sc} of 23.93 mA.cm-2, V_{OC} of 0.97V, and FF of 71%) and 14.65% (Jsc of 23.15 $mA.cm^{-2}$, V_{OC} of 0.96V, and FF of 65%), respectively.

Finally, we compared the intrinsic and operational stability of undoped, $BA_2FAPb_2I_7$-templated, and MACl-doped $FAPbI_3$ films and devices. The 2D-templated $FAPbI_3$ was exceptionally stable under a variety of conditions compared to both undoped and MACl-doped

$FAPbI_3$. The shelf stability of 2D-stabilized $FAPbI_3$ films showed a significant improvement compared to undoped $FAPbI_3$ (**Fig. S28**). We also performed in-situ GIWAXS measurements (**Fig. S29)** to compare the stability of MACl-doped and $BA_2FAPb_2I_7$-incorporated $FAPbI_3$ devices in a >90%RH environment at 65°C with 1-Sun illumination. The 2D-templated $FAPbI_3$ device showed minimal $\alpha \rightarrow \delta$ conversion over 170 min in the degrading environment. In contrast, the δ-phase became dominant in the MACl-doped $FAPbI_3$ device within the first 15 min of measurement. The much higher stability of the 2D-templated $FAPbI_3$ device in this experiment corroborated the maximum power point tracking (MPPT) device stability tests shown in **Fig. 5D** for 2D-templated $FAPbI_3$ and MACl-doped $FAPbI_3$.

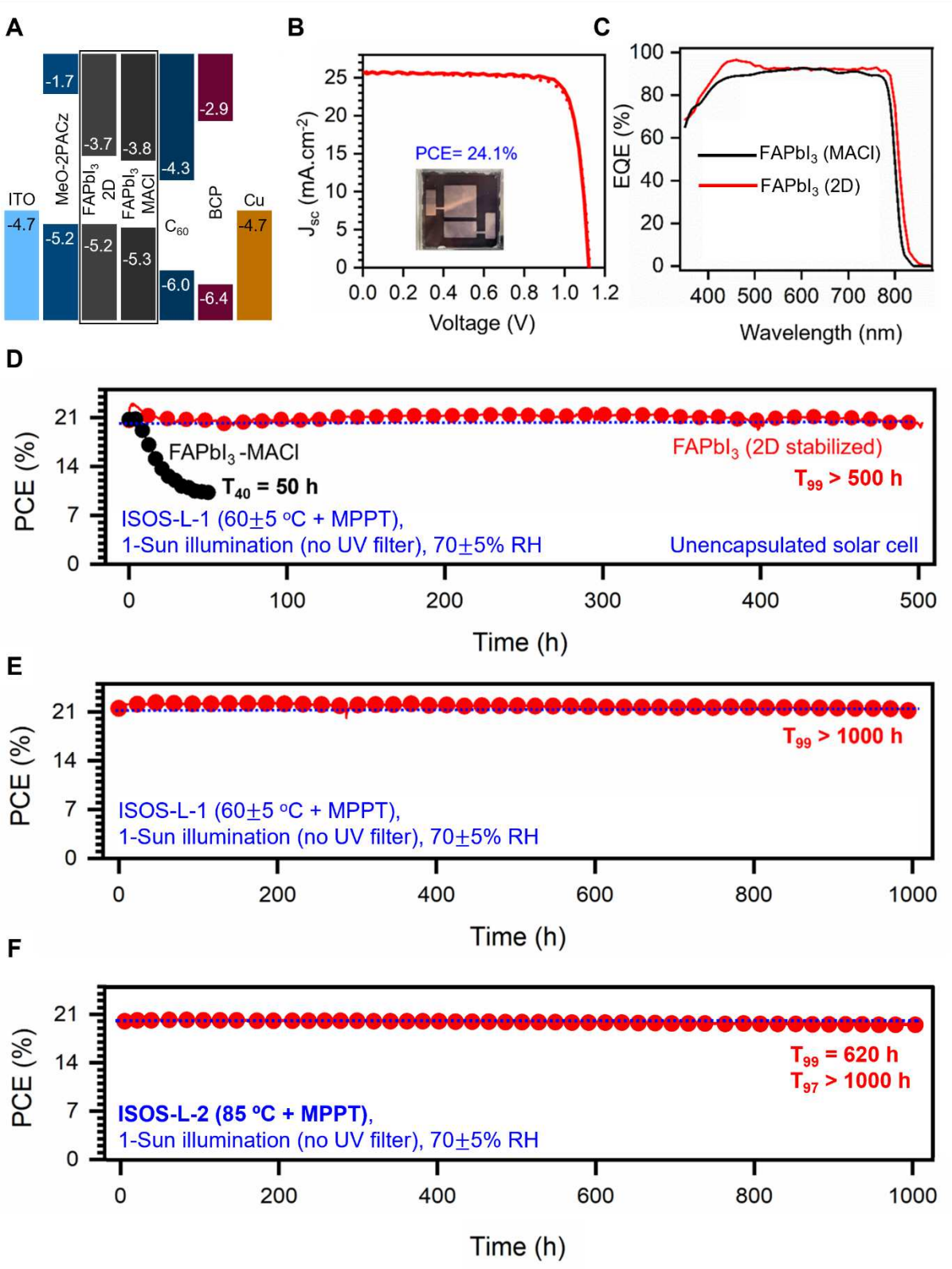

Figure 5: 2D-stabilized $FAPbI_3$ device performance. A) Device architecture of best-performing device showing band alignment of each layer. **B**) The J-V curve of the champion device shows

both a forward sweep (solid line) and reverse sweep (dashed line). The inset shows a real image of the device. **C**) The EQE of the champion 2D-stabilized $FAPbI_3$ device compared to the champion MACl-stabilized $FAPbI_3$ device. **D-F**) Stability tests on 2D stabilized $FAPbI_3$. **D**) Unencapsulated 2D-$FAPbI_3$ (red) and MACl-$FAPbI_3$ (black) cell under 1-sun illumination at 60ºC with MPP tracking, in ambient air. **E**) Encapsulated cell under 1-sun illumination at 60ºC with MPP tracking. **F**) Encapsulated cell under 1-sun illumination at 85ºC with MPP tracking.

We evaluated the device stability with standard interfaces. We first performed measurements on unencapsulated p-i-n solar cells in ambient air under 1-Sun illumination (no UV filter) with MPPT. As shown in **Fig. 5D**, the 2D-templated devices showed almost no PCE drop during the first 500 hours of operation with T_{99}>500 h. In contrast, the unencapsulated MACl-doped $FAPbI_3$ sample degraded within the first 50 hr of operation showing a T_{40}=50 h. Further, as shown in **Fig. 5E**, an encapsulated 2D-templated $FAPbI_3$ device showed almost no efficiency drop from an initial 21% PCE for more than 1000 hours (T_{99}>1000 hr) of continuous 1-Sun illumination at MPPT in ambient air (ISOS-L-1 protocol). This stability is among the best reported for $FAPbI_3$-based perovskite devices, which in recent reports *(26,27,36)* have been measured under inert conditions.

The encapsulated solar cells were additionally measured under 1-sun illumination at MPPT at 85°C on a hot plate in the ambient atmosphere (ISOS-L-2 protocol), as shown in **Fig. 5F**. The 2D-stabilized $FAPbI_3$ devices retained 99% of their initial PCE after 620 hours, and more than 97% of their initial PCE after 1000 hours. Using the rule of thumb from Si photovoltaics that a 10ºC increase in temperature translates to a 2x increase in degradation rate *(64)*, a T_{97} = 1000 hours at 85ºC corresponds to a T_{97} = 16000 hours (1.8 years) at 45ºC. This result is a critical step towards a $FAPbI_3$-based device with commercially-relevant stability.

Discussion

In summary, our investigation unveils a unique approach to achieve a highly stable black phase of $FAPbI_3$, even at temperatures considerably lower than the δ-$FAPbI_3$ to α-$FAPbI_3$ transition temperature. This method involves templating the (001) interplanar spacing of 3D $FAPbI_3$ to the (011) interplanar spacing of carefully selected 2D perovskites with FA as the cage cation, considering the respective Pb-Pb interatomic spacing for each structure. Detailed characterization, incorporating correlated WAXS, optical absorbance, and PL, indicates that the resulting black $FAPbI_3$ phase exhibits a lattice constant corresponding to the $d_{(011)}$ interplanar spacing of the underlying 2D perovskite. We extend this templating strategy to scalable solution-processed methods by introducing pre-synthesized 2D perovskite seeds to $FAPbI_3$ precursor solutions. During the film formation, the phase-stable 2D perovskite nucleates first due to its lower enthalpy of formation and stability at room temperature. The 2D structure acts as a seed on which the 3D perovskite to adopt the underlying 2D lattice periodicity, allowing for the preferential templating of the 3D perovskite on the 2D phase during subsequent film annealing. The resulting bulk $FAPbI_3$ films exhibit an energy gap (E_g) of 1.48 eV and demonstrate exceptional durability under aggressive conditions, achieving a remarkable PCE of 24.1% in a p-i-n device architecture on a 0.5 cm^2 device area. These outcomes validate a novel design strategy for the templated growth of 3D perovskites using 2D perovskites and will enable new physical behaviours and properties and functionalities relevant for optoelectronic devices. We anticipate that such strategies might extend beyond perovskites, potentially using other molecular and organic systems with comparable lattice constants to produce epitaxial kinetically stabilized materials.

558 REFERENCES
559

560 1. Masi, S., Gualdrón-Reyes, A. F. & Mora-Seró, I. Stabilization of Black Perovskite Phase in FAPbI3
561 and CsPbI3. *ACS Energy Lett.* **5**, 1974–1985 (2020).
562 2. Huang, Y. *et al.* The intrinsic properties of FA(1−x)MAxPbI3 perovskite single crystals. *J. Mater.*
563 *Chem. A* **5**, 8537–8544 (2017).
564 3. Tao, S. *et al.* Absolute energy level positions in tin-and lead-based halide perovskites. *Nature*
565 *communications* **10**, 2560 (2019).
566 4. Zhao, X.-G., Dalpian, G. M., Wang, Z. & Zunger, A. Polymorphous nature of cubic halide perovskites.
567 *Phys. Rev. B* **101**, 155137 (2020).
568 5. Stoumpos, C. C., Malliakas, C. D. & Kanatzidis, M. G. Semiconducting Tin and Lead Iodide
569 Perovskites with Organic Cations: Phase Transitions, High Mobilities, and Near-Infrared
570 Photoluminescent Properties. *Inorg. Chem.* **52**, 9019–9038 (2013).
571 6. Kawachi, S. *et al.* Structural and Thermal Properties in Formamidinium and Cs-Mixed Lead Halides.
572 *J. Phys. Chem. Lett.* **10**, 6967–6972 (2019).
573 7. Kieslich, G., Sun, S. & Cheetham, A. K. An extended tolerance factor approach for organic–inorganic
574 perovskites. *Chemical science* **6**, 3430–3433 (2015).
575 8. Ferreira, A. C. *et al.* Elastic softness of hybrid lead halide perovskites. *Physical Review Letters* **121**,
576 085502 (2018).
577 9. Li, Z. *et al.* Stabilizing perovskite structures by tuning tolerance factor: formation of formamidinium
578 and cesium lead iodide solid-state alloys. *Chemistry of Materials* **28**, 284–292 (2016).
579 10. Saliba, M. *et al.* Cesium-containing triple cation perovskite solar cells: improved stability,
580 reproducibility and high efficiency. *Energy & environmental science* **9**, 1989–1997 (2016).
581 11. Jeon, N. J. *et al.* Compositional engineering of perovskite materials for high-performance solar cells.
582 *Nature* **517**, 476–480 (2015).

12. Entropy-driven structural transition and kinetic trapping in formamidinium lead iodide perovskite | Science Advances. https://www.science.org/doi/10.1126/sciadv.1601650.
13. Green, M. A. *et al.* Solar cell efficiency tables (version 62). *Progress in Photovoltaics: Research and Applications* **31**, 651–663 (2023).
14. Min, H. *et al.* Perovskite solar cells with atomically coherent interlayers on SnO2 electrodes. *Nature* **598**, 444–450 (2021).
15. Yoo, J. J. *et al.* Efficient perovskite solar cells via improved carrier management. *Nature* **590**, 587–593 (2021).
16. Jeong, J. *et al.* Pseudo-halide anion engineering for α-FAPbI3 perovskite solar cells. *Nature* **592**, 381–385 (2021).
17. Kim, M. *et al.* Conformal quantum dot–SnO2 layers as electron transporters for efficient perovskite solar cells. *Science* **375**, 302–306 (2022).
18. Jeong, M. J. *et al.* Boosting radiation of stacked halide layer for perovskite solar cells with efficiency over 25%. *Joule* **7**, 112–127 (2023).
19. Park, J. *et al.* Controlled growth of perovskite layers with volatile alkylammonium chlorides. *Nature* 1–3 (2023) doi:10.1038/s41586-023-05825-y.
20. Zhao, Y. *et al.* Inactive (PbI2)2RbCl stabilizes perovskite films for efficient solar cells. *Science* **377**, 531–534 (2022).
21. Jiang, Q. *et al.* Surface reaction for efficient and stable inverted perovskite solar cells. *Nature* **611**, 278–283 (2022).
22. Li, Z. *et al.* Organometallic-functionalized interfaces for highly efficient inverted perovskite solar cells. *Science* **376**, 416–420 (2022).
23. Zhu, Z. *et al.* Correlating the perovskite/polymer multi-mode reactions with deep-level traps in perovskite solar cells. *Joule* **6**, 2849–2868 (2022).
24. Li, G. *et al.* Highly efficient p-i-n perovskite solar cells that endure temperature variations. *Science* **379**, 399–403 (2023).

25. Kim, M. *et al.* Methylammonium Chloride Induces Intermediate Phase Stabilization for Efficient Perovskite Solar Cells. *Joule* **3**, 2179–2192 (2019).
26. Min, H. *et al.* Efficient, stable solar cells by using inherent bandgap of α-phase formamidinium lead iodide. *Science* **366**, 749–753 (2019).
27. Park, B. *et al.* Stabilization of formamidinium lead triiodide α-phase with isopropylammonium chloride for perovskite solar cells. *Nat Energy* **6**, 419–428 (2021).
28. Hui, W. *et al.* Stabilizing black-phase formamidinium perovskite formation at room temperature and high humidity. *Science* **371**, 1359–1364 (2021).
29. Lee, J.-W., Seol, D.-J., Cho, A.-N. & Park, N.-G. High-Efficiency Perovskite Solar Cells Based on the Black Polymorph of HC(NH2)2PbI3. *Advanced Materials* **26**, 4991–4998 (2014).
30. Kim, G. *et al.* Impact of strain relaxation on performance of α-formamidinium lead iodide perovskite solar cells. *Science* **370**, 108–112 (2020).
31. Park, Y. H. *et al.* Inorganic Rubidium Cation as an Enhancer for Photovoltaic Performance and Moisture Stability of HC(NH2)2PbI3 Perovskite Solar Cells. *Advanced Functional Materials* **27**, 1605988 (2017).
32. Alanazi, A. Q. *et al.* Benzylammonium-Mediated Formamidinium Lead Iodide Perovskite Phase Stabilization for Photovoltaics. *Advanced Functional Materials* **31**, 2101163 (2021).
33. Alanazi, A. Q. *et al.* Atomic-Level Microstructure of Efficient Formamidinium-Based Perovskite Solar Cells Stabilized by 5-Ammonium Valeric Acid Iodide Revealed by Multinuclear and Two-Dimensional Solid-State NMR. *J. Am. Chem. Soc.* **141**, 17659–17669 (2019).
34. Hu, R. *et al.* Enhanced stability of α-phase FAPbI 3 perovskite solar cells by insertion of 2D (PEA) 2 PbI 4 nanosheets. *Journal of Materials Chemistry A* **8**, 8058–8064 (2020).
35. Huang, Y. *et al.* Low-Temperature Phase-Transition for Compositional-Pure α-FAPbI3 Solar Cells with Low Residual-Stress and High Crystal-Orientation. *Small Methods* **6**, 2200933 (2022).
36. Lee, J.-W. *et al.* 2D perovskite stabilized phase-pure formamidinium perovskite solar cells. *Nat Commun* **9**, 3021 (2018).

635 37. Liang, J. *et al.* Volatile 2-Thiophenemethylammonium and Its Strongly Bonded Condensation Product
636 for Stabilizing α-FAPbI3 in Sequential-Deposited Solar Cells. *ACS Materials Lett.* **5**, 1395–1400
637 (2023).
638 38. Liang, J. *et al.* Volatile 2D Ruddlesden-Popper Perovskite: A Gift for α-Formamidinium Lead
639 Triiodide Solar Cells. *Advanced Functional Materials* 2207177 (2022).
640 39. Shen, C. *et al.* Stabilizing Formamidinium Lead Iodide Perovskite by Sulfonyl-Functionalized
641 Phenethylammonium Salt via Crystallization Control and Surface Passivation. *Solar RRL* **4**, 2000069
642 (2020).
643 40. Shi, P. *et al.* Oriented nucleation in formamidinium perovskite for photovoltaics. *Nature* 1–5 (2023)
644 doi:10.1038/s41586-023-06208-z.
645 41. Sidhik, S. *et al.* Memory Seeds Enable High Structural Phase Purity in 2D Perovskite Films for High-
646 Efficiency Devices. *Adv. Mater.* **33**, 2007176 (2021).
647 42. Sidhik, S. *et al.* High-phase purity two-dimensional perovskites with 17.3% efficiency enabled by
648 interface engineering of hole transport layer. *Cell Reports Physical Science* **2**, 100601 (2021).
649 43. Metcalf, I. *et al.* Synergy of 3D and 2D Perovskites for Durable, Efficient Solar Cells and Beyond.
650 *Chem. Rev.* **123**, 9565–9652 (2023).
651 44. Hou, J., Li, W., Zhang, H., Sidhik, S., Fletcher, J., Metcalf, I., Anantharaman, S.B., Shuai, X., Mishra,
652 A., Blancon, J.C. and Katan, C. Synthesis of 2D perovskite crystals via progressive transformation of
653 quantum well thickness. *Nature Synthesis*, **pp.1-11,** (2023).
654 45. Blancon, J.-C., Even, J., Stoumpos, Costas. C., Kanatzidis, Mercouri. G. & Mohite, A. D.
655 Semiconductor physics of organic–inorganic 2D halide perovskites. *Nat. Nanotechnol.* **15**, 969–985
656 (2020).
657 46. Blancon, J.-C. *et al.* Extremely efficient internal exciton dissociation through edge states in layered 2D
658 perovskites. *Science* **355**, 1288–1292 (2017).
659 47. Blancon, J.-C. *et al.* Scaling law for excitons in 2D perovskite quantum wells. *Nat Commun* **9**, 2254
660 (2018).

48. Stoumpos, C. C. *et al.* Ruddlesden–Popper Hybrid Lead Iodide Perovskite 2D Homologous Semiconductors. *Chem. Mater.* **28**, 2852–2867 (2016).
49. Even, J., Pedesseau, L. & Katan, C. Understanding quantum confinement of charge carriers in layered 2D hybrid perovskites. *ChemPhysChem* **15**, 3733–3741 (2014).
50. Tamarat, P. *et al.* Universal scaling laws for charge-carrier interactions with quantum confinement in lead-halide perovskites. *Nature Communications* **14**, 229 (2023).
51. Sapori, D., Kepenekian, M., Pedesseau, L., Katan, C. & Even, J. Quantum confinement and dielectric profiles of colloidal nanoplatelets of halide inorganic and hybrid organic–inorganic perovskites. *Nanoscale* **8**, 6369–6378 (2016).
52. Katan, C., Mercier, N. & Even, J. Quantum and dielectric confinement effects in lower-dimensional hybrid perovskite semiconductors. *Chemical reviews* **119**, 3140–3192 (2019).
53. Song, S. *et al.* Molecular Engineering of Organic Spacer Cations for Efficient and Stable Formamidinium Perovskite Solar Cell. *Advanced Energy Materials* **10**, 2001759 (2020).
54. Doherty, T. A. S. *et al.* Stabilized tilted-octahedra halide perovskites inhibit local formation of performance-limiting phases. *Science* **374**, 1598–1605 (2021).
55. Beal, R. E. *et al.* Structural Origins of Light-Induced Phase Segregation in Organic-Inorganic Halide Perovskite Photovoltaic Materials. *Matter* **2**, 207–219 (2020).
56. Winarski, R. P. *et al.* A hard X-ray nanoprobe beamline for nanoscale microscopy. *J Synchrotron Rad* **19**, 1056–1060 (2012).
57. Li, N. *et al.* Microscopic degradation in formamidinium-cesium lead iodide perovskite solar cells under operational stressors. *Joule* **4**, 1743–1758 (2020).
58. Weber, O. J. *et al.* Phase Behavior and Polymorphism of Formamidinium Lead Iodide. *Chem. Mater.* **30**, 3768–3778 (2018).
59. Ungár, T. Microstructural parameters from X-ray diffraction peak broadening. *Scripta Materialia* **51**, 777–781 (2004).

60. Li, Y. *et al.* CH3NH3Cl Assisted Solvent Engineering for Highly Crystallized and Large Grain Size Mixed-Composition (FAPbI3)0.85(MAPbBr3)0.15 Perovskites. *Crystals* **7**, 272 (2017).
61. Ye, F. *et al.* Roles of MACl in Sequentially Deposited Bromine-Free Perovskite Absorbers for Efficient Solar Cells. *Advanced Materials* **33**, 2007126 (2021).
62. Zacharias, M., Volonakis, G., Giustino, F. & Even, J. Anharmonic electron-phonon coupling in ultrasoft and locally disordered perovskites. *npj Comput Mater* **9**, 1–13 (2023).
63. Alam, M. A. & Khan, M. R. *Principles of solar cells: connecting perspectives on device, system, reliability, and data science*. (World Scientific Publishing Co. Pte. Ltd, 2022).
64. Boyd, C. C., Cheacharoen, R., Leijtens, T. & McGehee, M. D. Understanding Degradation Mechanisms and Improving Stability of Perovskite Photovoltaics. *Chem. Rev.* **119**, 3418–3451 (2019).

Acknowledgements

In situ diffraction experiments were conducted at the Advanced Light Source, beamline 12.3.2 supported by Nobumichi Tamura, which is a US Department of Energy Office of Science User Facility under contract no. DE-AC02-05CH11231. The authors thank Jonathan Slack from the ALS for development and maintenance of the in-situ spin coater. The authors are grateful to Tanguy Terlier for the measurement and analysis of ToF-SIMS data.

Funding:

The work Rice University was supported by the DOE-EERE DE-EE0010738 program. I.M. acknowledges the financial support from the Hertz Foundation and the National Science Foundation Graduate Research Fellowship Program (This material is based upon work supported by the National Science Foundation Graduate Research Fellowship Program under grant no. NSF 20-587. Any opinions, findings and conclusions or recommendations expressed in this material are those of the author and do not necessarily reflect the views of the National Science Foundation). A.B. was supported by a fellowship through the National Science and Engineering Graduate Fellowship Program (NDSEG) sponsored by the Air Force Research Laboratory (AFRL), the Office of Naval Research (ONR), and the Army Research Office (ARO). J.H. acknowledges the financial support from the China Scholarship Council (No. 202107990007). J.E. acknowledges the financial support from the Institut Universitaire de France. Work at the Molecular Foundry was supported by the Office of Science, Office of Basic Energy Sciences, of the U.S. Department of Energy under Contract No. DE-AC02-05CH11231. T. K. acknowledges funding by the German Science Foundation (DFG, fellowship number KO6414).

Authors contributions:

A.D.M., and J.E. conceived the idea, designed the experiments, analyzed the data, and cowrote the manuscript. S.S., W.L., and I.M., designed experiments, analyzed the data and co-wrote the manuscript. S.S. Fabricated devices, tested devices, performed templating experiments, performed WAXS measurements, performed in-situ PL measurements, performed stability experiments. I.M. Fabricated devices, tested devices, synthesized 2D crystals, performed WAXS measurements, performed GIWAXS measurements, performed in-situ PL measurements. W.L. and E.T. performed and analyzed the GIWAXS measurements. T.K. performed WAXS measurements, performed in-situ PL measurements under the guidance of C.M.S-F. C.D. and A.T. performed nano-XRD measurements and analyzed the data under the guidance from D.F. M.K. performed the Dynamic Light Scattering of $FAPbI_3$ solutions under the guidance from A.B.M. J. H. synthesized the 2D perovskite crystals. F.M., R.P., and R.G. fabricated devices, tested devices and helped in performing the stability experiments. H.Z. Performed ex-situ optical measurements with the help from A.T. I.A.M.P. performed and analyzed the ss-NMR measurements under the guidance of G.N.M.R. A.B. performed the PES measurements for the perovskite thin films under the guidance of M.G.K. M.A.A. analyzed device performance. C.K. analyzed the structural properties of 2D and lattice mismatch between the 2D and 3D. D.G. analyzed the optical spectroscopy measurements and contributed to editing the paper.

Competing interests: The authors declare no competing interests.

Data and Materials Availability: All (other) data needed to evaluate the conclusions in the paper are present in the paper or the Supplementary Materials.

Supplementary Information

Two-dimensional perovskite templates for durable and efficient formamidinium perovskite solar cells

Siraj Sidhik[1,2#], Isaac Metcalf[1#], Wenbin Li[3], Tim Kodalle[4], Connor Dolan[5], Mohammad Khalili[2], Jin Hou[1], Faiz Mandani[2], Andrew Torma[3], Hao Zhang[3], Jessica Persaud[2], Amanda Marciel[2], Itzel Alejandra Muro Puente[6], G. N. Manjunatha Reddy[6], Adam Balvanz[7], Mohamad A. Alam[8], Claudine Katan[9], Esther Tsai[10], David Ginger[11], David Fenning[5], Mercouri G. Kanatzidis[12], Carolin M. Sutter-Fella[4], Jacky Even[13]* and Aditya D. Mohite[1,2]*

1. Methods and Characterization

1.1 High purity 2D perovskite powder synthesis

We synthesized the 2D Ruddlesden-Popper perovskite parent crystals, $BA_2FAPb_2I_7$ by combining the lead oxide (PbO, Sigma Aldrich, 99%), formamidine hydrochloride (FACl, Sigma Aldrich, ≥98%), and butylamine (BA, Sigma Aldrich, 99.5%) in precise stoichiometric ratios. This mixture was dissolved in a solution of hydroiodic acid (HI, 57 wt% in H2O) and hypophosphorous acid (H_3PO_2, 50% in H_2O) and stirred at a temperature of 240°C until complete dissolution of the precursor materials and boiling of the solution occurred. Subsequently, the precursor solution was allowed to cool down to room temperature, resulting in the crystallization of flat single crystals with sizes ranging from micrometres to millimetres. To ensure the quality and phase purity of the synthesized crystals, we performed a comprehensive analysis using a combination of X-ray diffraction and absorbance measurements.

1.2 Air-liquid interface method for single crystal growth of $BA_2FAPb_2I_7$

To synthesize large-area 2D Ruddlesden-Popper perovskite crystals, $BA_2FAPb_2I_7$, we combine lead oxide (PbO, Sigma Aldrich, 99%), formamidine hydrochloride (FACl, Sigma Aldrich, ≥98%), and butylamine (BA, Sigma Aldrich, 99.5%) in precise stoichiometric ratios. This mixture is dissolved in a solution of hydroiodic acid (HI, 57 wt% in H2O) and hypophosphorous acid (H3PO2,

50% in H2O), and stirred at a temperature of 240°C until the precursor materials completely dissolve and the solution begins to boil. Subsequently, the solution is kept at a temperature of 100˚C without stirring. A clean glass is introduced at the bottom of the vial, allowing the large-area crystals to form at the air-liquid interface. Once the crystal has formed, the glass is carefully extracted from the vial using forceps, with the slightest movement aiding in scooping up the formed crystals. The resulting film on the glass is washed with ether and annealed at a temperature of 125°C to remove any trapped solvents in the crystals.

1.3 Solar cell fabrication

Inverted planar perovskite solar cells: The patterned glass/ITO substrates underwent a sequential cleaning process involving ultrasonication in soap water, followed by deionized water, acetone, and a mixture of acetone and ethanol (1:1), each for 15 minutes. After drying the substrates and subjecting them to 30 minutes of UV-ozone cleaning, they were transferred to a glove box. Inside the glove box, a hole-transporting layer (HTL) with a thickness of approximately 10 nm was created using the SAMs layer (MeO-2PACz, TCI, America) at a concentration of 0.8 mg/ml in Ethanol. The HTL was deposited by spin coating at 5000 rpm for 30 seconds, followed by annealing at 100 ˚C for 10 minutes.

To prepare the $FAPbI_3$ perovskite precursor solution with a concentration of 1.0 M, the PbI_2, and FAI, were mixed in a solvent mixture of DMF and DMSO (6:1). The solution was continuously stirred for 4 h, following which various mol% of the formamidinium based 2D perovskite, $A'_2FA_{n-1}Pb_nI_{3n+1}$, where A' stands for different bulky organic cations such as butylammonium, and pentylammonium etc, was introduced and left for aging on the hot plate at 70^{o}C for 30 min. A single-step spin coating process was employed to achieve a uniform coverage of the perovskite film by spin coating the solution at 5000 rpm for 30 seconds with an acceleration

of 2500 rpm/s. The samples were subsequently annealed at 150 ˚C for 20 minutes. Lastly, the devices were completed by thermal evaporation of C60 (30 nm), BCP (1 nm), and Copper (100 nm) under a vacuum of less than $2x10^{-6}$ torr. The active area selected for the devices was 0.5 cm^2.

1.4 Optical absorbance and photoluminescence measurements

Thin film absorbance measurements: Film absorbance measurements were carried out using a setup that involved illuminating the samples with modulated monochromatic light at a frequency of 2 kHz. The light was generated by a quartz-tungsten-halogen light source and passed through a monochromator (SpectraPro HRS 300, Princeton Instruments). To detect the transmitted light, synchronous detection was employed using a silicon photodiode connected to an SR865 lock-in amplifier. The measurements were conducted in the spectral range of 400 – 800 nm, with a dwell time of 0.1 s for each data point. Throughout the experiment, the samples were maintained under vacuum conditions of approximately 10^{-4} torr and kept at room temperature.

Steady-state photoluminescence measurements: Thin-film photoluminescence (PL) measurements were performed using a lab-built confocal microscopy system to acquire steady-state photoluminescence (SS-PL) data. Spectra were collected using an Andor Kymera 329i spectrometer and an Andor iDus 416 CCD detector. The acquired spectra were then processed using Savitzky-Golay filtering for optimal signal-to-noise ratio. For photoexcitation, the samples were illuminated with a monochromatic pulsed laser emitting at 2.58 eV (480 nm). The laser, with a pulse duration of 6 ps and a repetition rate of 78.1 MHz, was focused near the diffraction limit, achieving a resolution of approximately 0.5 µm. The excitation intensity was carefully adjusted to 360 W/cm^2. PL measurements were conducted in the spectral range of 450 - 900 nm with a dwell time of 0.1 s. The experiments were performed under vacuum conditions (10^{-5} torr) at room temperature. PL maps were acquired by scanning a region of either 40 µm x 40 µm or 100 µm x

100 μm, using a step size of 1 μm. At each step, the peak position of the photoluminescence signal was extracted and recorded for further analysis.

1.5 Time-resolved photoluminescence (TRPL) measurements

Time resolved photoluminescence (TRPL) measurements were performed by exciting the samples with various fluence laser pulse (420 nm, 40 fs pulse duration and 100 kHz repetition rate). These laser pulses are generated by frequency doubling the laser pulse from diode-pumped Yb:KGW femtosecond laser system (PHAROS) using barium-beta-borate crystal. This laser pulse (beam spot size of 20 μm) was then focused onto sample with a 3.8 mm focal length lens. The emitted light was then collected using a Mitutoyo objective lens (numerical aperture = 0.7, magnification = 100×) from the transmission side and subsequently spatially filtered using a mechanical iris located at the conjugate plane. Elastically scattered light was rejected by using a long pass filter (wavelength 650 nm, optical density = 6.0). Additionally, bandpass filter centred at 800 nm (wavelength = 800±20 nm, optical density = 4.0) was employed to filter the emitted light. The emitted light was then focused onto the Micro Photon Device (MPD) PDM series single-photon avalanche photodiode with an active area of 50 μm. The temporal resolution was set at a binning size of 64 ps. Photoluminescence spectra were collected by directing the emitted light towards a spectrometer using a flippable mirror.

1.6 Ultrafast Transient absorption spectroscopy

Time-resolved absorption (TA) data of the samples were obtained using transient femtosecond pump-probe spectroscopy. The samples were excited by 420 nm laser pulse generated by using an optical parametric amplifier having a pulse duration of 40 fs and a beam spot size of 120 μm. Diode-pumped Yb: KGW femtosecond laser system based on the principle of chirped-pulse amplification (PHAROS) produces light pulses centred at 840 nm. These laser pulses were then

passed through 0.5 mm thick barium-beta-borate crystal where the frequency will be doubled to produce laser pulses centred at 420 nm acting as pump pulse. These laser pulses are focused on the sample with a spot size of 120 μm in diameter ($1/e^2$). Another laser pulse from the amplifier is focused onto a sapphire crystal to produce white-light supercontinuum that acts as a probe pulse. The optical path length between pump and probe is manipulated by passing the probe beam through a retroreflector mounted on high precision motorized translational stage. Probe pulse (beam diameter 35 μm) was then focused and spatially overlapped with the pump pulse onto the sample. It is then re-collimated and directed onto a multi-mode fibre for wavelength-sensitive detection.

1.7 X-ray diffraction measurements

1D X-ray diffraction of the 3D perovskite thin films were measured in the 2θ between 2˚ and 30˚, with a step of 0.01˚ and a speed of 2º/min, using a Rigaku SmartLab X-Ray diffractometer with Cu(K**α**) radiation (λ = 1.5406 Å). For lattice parameter determination shown in **Figure 2E**, thin films were scraped with a blade and wiped onto a glass slide to remove any residual strain from the substrate. The scraped films were then coated with a thin film of PMMA to prevent α → δ conversion during XRD measurement in air.

Single crystal X-Ray diffraction of the 2D perovskite crystals was taken with a Rigaku Synergy-S diffractometer using a Mo target. The temperature was held at 300K.

1.8 Differential Scanning Calorimetry (DSC) measurements

$FAPbI_3$ powders for DSC were prepared by spin-coating 300μL of $FAPbI_3$ precursor solution onto a large-area ($25cm^2$) substrate, drying at room temperature under vacuum, and scraping with a blade. DSC was performed using a TA DSC 250 with a scan rate of 1ºC/min.

1.9 Nuclear Magnetic Resonance (NMR) measurements

$FAPbI_3$ powders for NMR were prepared by spin-coating 300µL of $FAPbI_3$ precursor solution onto a large-area ($25cm^2$) substrate, annealing, and scraping with a blade. Powders were dissolved in 600 µL of deuterated DMSO. ^1H NMR was performed on a 600 MHz Bruker NEO Digital NMR Spectrometer. For ^1H NMR a higher BA n=2 concentration of 5 mol% was employed to better resolve the butylammonium signal. For solid-state NMR measurements, thin films of control 2D and 2D-doped $FAPbI_3$ were deposited on glass substrates, scraped with a blade, and collected as a powder. To minimize the material degradation during solid-state NMR data collection, the materials were separately packed into air-tight and opaque zirconia rotors (1.3 mm, outer diameter) fitted with VESPEL caps. All ex-situ solid-state MAS NMR experiments were conducted at 21.1 T (Larmor frequency ^1H = 900 MHz). The MAS frequency was 50 kHz in all ssNMR experiments. ^1D 1H MAS NMR spectra were acquired by co-addition of 16 transients. An interscan delay was set to 45 s, as determined from saturation recovery measurements and analyses, to ensure the full T_1 relaxation and hence the quantitative proton peak intensities. 2D ^1H-^1H spin diffusion NMR experiments were acquired using a three-pulse NOESY-like sequence with 500 µs of mixing time for the α-$FAPbI_3$-low dimensional phase (BA or PA). A rotor-synchronized increment of 20 µs was applied to detect 400 T_1 increments, each with 2 co-added transients. For all materials, the ^1H experimental shift was calibrated with respect to neat TMS using adamantane as an external reference (^1H resonance, 1.81 ppm).

From 1D ^1H ssNMR spectra of precursor compounds, control 2D materials and 2D-doped $FAPbI_3$ materials (**Figure S15A-B**), the ^1H peaks corresponding to the different organic cations can be identified and distinguished. For reference, the ^1H signals of the FA^+ is attained (blue boxes), and BA^+ signals in the BA-stabilized perovskite can be found in the orange box, and BA^+ signals in the BA-stabilized perovskite are presented in the purple box. The origin of these signals is

885 further corroborated by acquiring the ^{1}H ssNMR spectra of neat 2D $BA_2FAPb_2I_7$ and $PA_2FAPb_2I_7$
886 phases. The comparison of the ^{1}H peak integrals associated with the of FA^+ and BA^+ suggests that
887 there is ~7.9 mol% of 2D phase present in the 3D phase, which is estimated to be ~7.9 mol% for
888 the 2D $PA_2FAPb_2I_7$ doped material.

889 To gain insights into the local proximities between the BA cations and the FA cations in
890 the 2D $BA_2FAPb_2I_7$ /$PA_2FAPb_2I_7$ doped $FAPbI_3$ phases, 2D ^{1}H-^{1}H spin-diffusion (SD) NMR
891 experiments were carried out and analyzed. Specifically, magnetization exchange between dipolar
892 coupled spins (here protons) allows the through-space proximities between neighboring sites, for
893 example, information on through-space ^{1}H-^{1}H proximities in different organic cations to be probed.
894 In 2D ^{1}H-^{1}H SD spectra, the on-diagonal peaks provide information on chemical shifts and the off-
895 diagonal peaks contain information on spin magnetization exchange between chemically
896 inequivalent spins. For both BA and PA-stabilized 3D phases, a mixing delay of 50 μs was
897 insufficient to produce off-diagonal peaks, but a mixing delay of 500 μs leads to the magnetization
898 exchange between the ^{1}H sites in in BA^+, FA^+ and between BA^+/FA^+ and PA^+/FA^+ as seen in green
899 and gray boxes, respectively **(Figure S15E-F)**. These peaks indicate the coexistence of a mixed
900 2D/3D phase. Relatively strong intensity peaks observed for the BA-stabilized $FAPbI_3$ phase
901 suggesting that the high degree of mixing of 2D phase within the 3D phase, as compare to the PA-
902 stabilized $FAPbI_3$. In addition, the peaks with in the purple and orange boxes indicate the close
903 proximities between the proton sites within PA and BA cations respectively.
904

905 **1.10 Time-of-Flight Secondary Ion Mass Spectrometry (ToF-SIMS) measurements**

906 Positive high mass resolution depth profiles were conducted using a combined TOF-SIMS NCS
907 instrument, which integrates a TOF.SIMS instrument (ION-TOF GmbH, Münster, Germany) and

908 an in-situ Scanning Probe Microscope (NanoScan, Switzerland) at the Shared Equipment
909 Authority from Rice University. The analysis field of view covered an area of 80 × 80 μm^2 (Bi^{3+}
910 at 30 keV, 0.35 pA) with a raster of 128 x 128 during the depth profile. To compensate for charge
911 effects, an electron flood gun was employed throughout the analysis. The charge effects were
912 adjusted using a surface potential of -36V and an extraction bias of 0V.

913 The cycle times were set at 90 μs, corresponding to a mass range of m/z = 0 – 735 a.m.u.
914 During sputtering, a raster of 450 × 450 μm^2 was used (Cs^+ @ 1 keV, 44 nA). The beams operated
915 in a non-interlaced mode, alternating between 1 analysis cycle and 1 frame of sputtering (taking
916 approximately 1.31s), followed by a 2-second pause for charge compensation. To enhance the
917 understanding of the data, MCs^{n+} (n = 1, 2) depth profiling was also employed. This method is
918 particularly useful for quantifying alloys and identifying ion compounds. The cesium primary
919 beam was utilized for sputtering during the depth profile, enabling the detection of MCs^+ or MCs^{2+}
920 cluster ions, where M represents the element of interest combined with one or two Cs atoms. The
921 use of MCs+ and MCs^{2+} ions in ToF-SIMS analysis offers several advantages, including the
922 reduction of matrix effects and the ability to detect compounds containing both electronegative
923 and electropositive elements. All depth profiles were point-to-point normalized based on the total
924 ion intensity, and the data were plotted using a 5-point adjacent averaging. The normalization and
925 smoothing techniques facilitated a better comparison of the data obtained from different samples.
926 Depth calibrations were established by measuring the thicknesses using a surface profiler, which
927 generated a line scan of the craters using in-situ SPM through contact scanning.

928 **1.11 In-situ WAXS measurements for $FAPbI_3$ film formation**

929 The experimental setup took place in a custom-made analytical chamber located at the
930 12.3.2 microdiffraction beamline of the Advanced Light Source. This specialized chamber was

931 designed to accommodate various measurements and processes simultaneously, including the
932 handling of thin films. The indium-doped tin oxide substrate, which had been cleaned using plasma,
933 was securely positioned on the integrated spin coating puck-heater and affixed with a heat transfer
934 paste. To initiate the deposition process, a liquid precursor containing 1 M PbI_2 and
935 formamidinium in a solvent mixture of 6:1 DMF:DMSO was carefully pipetted onto the substrate's
936 surface. To maintain a controlled environment, the chamber was sealed off from the external
937 surroundings and kept under a continuous nitrogen flow. The experiment proceeded by subjecting
938 the precursor to spin coating, which involved two steps: the first spin coating was carried out at
939 4000 rpm for 30 s to create a thin film. During the second spin coating step, precisely 10 s into the
940 process, a remotely controlled pipette dispensed a stream of ethyl acetate.

941 After the completion of the spin coating protocol, a remote heating protocol was initiated.
942 A nonlinear stepwise annealing sequence was applied, in which the substrate temperature was
943 increased by steps of 20°C in 20 sec intervals up to 100°C and then increased by steps of 25°C up
944 to 150°C. The temperature was then maintained at 150 °C for the duration of the experiment, which
945 lasted until t = 300 s. The incident X-ray beam was directed at an incidence angle of 1° with a beam
946 energy of 10 keV. The distance between the sample and detector, known as the sample detector
947 distance (SDD), was approximately 155 mm. The detector itself was positioned at an angle of 39°
948 relative to the sample plane. WAXS (wide-angle X-ray scattering) data were acquired with an
949 exposure time of 1.0 s and an additional pause of 0.8 s (total 1.8 s) between measurements using a
950 2D Pilatus 1 M detector (Dectris Ltd.). Photoluminescence excitation was achieved by utilizing a
951 532 nm Thorlabs diode-pumped solid-state laser with a power density of 40 mW/cm^2. The
952 resulting photoluminescence signal was collected by a lens, directed into an optical fiber, and
953 transmitted to a grating OceanOptics QE Pro spectrometer for detection. To regulate the annealing

954 temperature and protocol, a pre-calibrated Raytek MI3 pyrometer recorded the temperature of the
955 heating puck. The temperature control system utilized a pre-programmed PID loop.
956 *Calibration of peak positions during heating:* The heat transfer paste holding the substrate is
957 known to expand with temperature, changing the height of the substrate slightly. A change in
958 height also changes the sample-detector distance and the direct beam position with respect to the
959 detector, giving the illusion that peaks are shifting towards higher q-values as temperature
960 increases. It is best practice to correct for this height change over the temperature ramping with
961 regards to the principal ITO peak at q = 2.15 $Å^{-1}$. However, this peak overlaps with the (112)
962 diffraction peak from the $FAPbI_3$ δ – phase, which emergers once the antisolvent is deposited and
963 persists during temperature ramping. Instead, we compared the position of the principal ITO peak
964 at room temperature before antisolvent dropping with its position at 150ºC after the δ – phase had
965 converted to α – phase. We assumed a linear relation between temperature and change in substrate
966 height, which allowed us to use the in-situ temperature data to correct for this peak shift during
967 temperature ramping.
968
969 **1.12 Dynamic Light Scattering (DLS) measurements**
970 *Experimental methods:* The solutions of $FAPbI_3$+ $BA_2FAPb_2I_7$ perovskites were prepared by
971 dissolving precursors and high purity crystal powders in DMF as described in section S1.3 and
972 adding 5 and 10 mg of n=2 $BA_2FAPb_2I_7$. The prepared solutions were loaded into cylindrical glass
973 cuvettes (Wilmad® NMR tubes 5 mm diam., high throughput. 103 mm length). Dynamic Light
974 Scattering (DLS) measurements were performed immediately by capturing correlation curves at
975 four different angles: 60°, 90°, 120°, and 150°. The measurements were conducted at an ambient

976 temperature of 20°C using a fully automated 3D LS Spectrometer (LASER: 660 nm, 65 mW, LS
977 Instruments AG, Fribourg). Each angle was measured in triplets.
978 *Extraction of the size of the particles in solution:* Below is a detailed description of the analysis
979 conducted on the multi-angle Dynamic Light Scattering (DLS) data obtained from various
980 concentrations of precursor solutions. The autocorrelation curves were measured for each solution
981 to examine their angular dependence. These correlation curves were then fitted using a single-
982 exponential decay model. The residuals resulting from the correlation fitting were measured and
983 plotted. Furthermore, a linear regression of Γ versus q2 was performed, focusing on the range
984 between 60° and 150°. The scattered light correlation function, $g^{(2)}$, compares the intensity of
985 received signal between time t and later time t+τ,(*5*)

986 $$g^{(2)}(q,\tau) = \frac{<I(t)I(t+\tau)>}{<I(t)^2>} \quad (2)$$

987 Using the Siegert relationship that relates the field correlation function and intensity correlation
988 function given by(*6*)

989 $$g^{(2)}(q,\tau) - 1 = \beta\left|g^{(1)}(q,\tau)\right|^2 \quad (3)$$

990 where β is a constant proportional to the signal-to-noise ratio.

991 For a system undergoing Brownian motion the electric field correlation function is shown to decay
992 exponentially as

993 $$g^{(1)}(q,\tau) = exp\ (-\Gamma\tau) \quad (4)$$

994 When several groups of particles with different sizes (labelled *i*) are present in solution, the DLS
995 data can be fitted using(*6*):

$$g^{(2)}(q,\tau) - 1 = \sum_i \quad \alpha_i \left| g_i^{(1)}(q,\tau) \right|^2 = \sum_i \quad \alpha_i |exp\,(-\Gamma_i \tau)|^2 \qquad (5)$$

Then, for the group of particles i the value Γ_i is related to the translational diffusion coefficient $D_{T,i}$ and wave number q through.

$$\Gamma_i = D_{T,i} q^2 \qquad (6)$$

with,

$$q = \frac{4\pi\eta}{\lambda} sin\left(\frac{\theta}{2}\right) \qquad (7)$$

η is the refractive index of the solvent, λ is the wavelength of the laser, and θ the angle between the incident laser beam and the scattered light. Finally, the diffusion coefficient is related to the hydrodynamic radius R_{H} of particles in a Brownian motion by the Stokes-Einstein equation(*7*)

$$D_{T,i} = \frac{k_B T}{6\pi\mu R_{H,i}} \qquad (8)$$

with k_B is the Boltzmann constant, T the temperature, μ the dynamic viscosity, and $R_{H,i}$ the median hydrodynamic radius of the group *i* of particles.

1.13 Nano X-Ray diffraction measurements.

Nano X-ray Diffraction measurements were taken at the hard X-ray nanoprobe at Sector 26 ID-C of the Advanced Photon Source at Argonne National Laboratory. Samples were fabricated on X-ray transparent silicon nitride (Norcada, part no. NX5050D) windows for measurement in transmission geometry, enabling measurements at near-normal incidence and minimizing beam projection on the sample surface. Measurements were taken at 9.6 keV incident X-ray energy using an X-ray probe with a full width at half maximum of approximately 25 nm focused using a Fresnel zone plate and order-sorting aperture to minimize the probe broadening contribution of higher

order diffraction. Diffraction patterns were collected with a zero-noise diffraction CCD. Diffraction patterns were recorded using a Dectris Eiger2 single photon counting detector with 75 μm pixel width and angular resolution ranging from 0.018-0.023° per pixel at low and high two theta, respectively. Dwell times of 0.1 s per point were used to generate nano-diffraction maps. The X-ray diffraction pattern remained consistent for many seconds of X-ray irradiation at a single point, as determined by measuring X-ray diffraction patterns over time for all samples (**Figure S17**).

1.14 Grazing incidence wide angle X-ray scattering

Experimental methods: The GIWAXS (grazing-incidence wide-angle X-ray scattering) measurements presented in this paper were conducted at two different synchrotron beamlines: 8-ID-E at the Advanced Photon Source (APS) and 11-BM at the National Synchrotron Light Source-II (NSLS II). For experiments performed at beamline 8-ID-E, the samples were positioned on a specialized Linkam grazing incidence x-ray-scattering (GIXS) stage placed inside a vacuum chamber with a pressure of 10^{-4} torr. The Pilatus 1M (Dectris) area detector was situated approximately 228 mm away from the sample. A photon energy of 10.91 keV was employed, and the X-ray beam had a size of 200 μm × 20 μm (horizontal × vertical). On the other hand, experiments at beamline 11-BM utilized a robotic stage within a vacuum chamber maintained at a pressure of 6×10^{-2} torr. The sample-to-detector distance was approximately 267 mm, and the Pilatus 800K (Dectris) area detector was employed. The photon energy used was 13.5 keV, and the X-ray beam had dimensions of 200 μm × 50 μm (horizontal × vertical).

In-situ GIWAXS during degradation was performed using a solvent vapor annealing chamber in the open sample staging area at 11-BM. The measurement beam entered and exited the chamber through Kapton windows on either side. For high-humidity measurements, liquid

water was added to the bottom of the chamber to fix the atmosphere at >90%RH. For illuminated measurements, AM1.5G light entered the chamber from the top through a glass window. For heated measurements, a resistive heating element below the sample controlled the chamber temperature.

GIWAXS analysis: To analyze the GIWAXS patterns, a full angular integration was conducted to obtain a 1-D X-ray spectrum. The Debye-Scherrer formula was employed to determine the average grain size (D_{hkl}) of the perovskite thin film, where (hkl) represents the Miller indices. For the analysis of the 2D perovskite top film, the (200) plane was utilized, while the (001) plane was selected for the 3D perovskite film. The Scherrer equation incorporated a shape factor (K) of 0.9. The formula is presented as follows:

$$D_{hkl} = \frac{K\lambda}{\beta_{hkl} coscos\, \theta_{hkl}} \quad (1)$$

where λ is 1.1365 Å and is the X-ray wavelength, θ is the diffraction peak position, β is the full-with-at-half-max (FWHM). The FWHM was extracted by fitting the diffraction profile to a pseudo-Voigt function. The FWHM was correct for the geometry of the measurement such as the X-ray beam divergence, energy bandwidth, and the parallax effect of the beam footprint.

1.15 Thin-film morphology measurements

Scanning electron microscopy (SEM) measurements: The surficial and cross-sectional SEM images were acquired using the FEI Quanta 400 ESEM FEG instrument. The fabrication process involved depositing the 3D control and the 2D templated 3D perovskite films onto a Silicon substrate, followed by sputtering approximately 15 nm of gold to improve film conductivity. The SEM images were captured at a voltage of 12.5 kV, and a dwell time of 30 μs was utilized during image acquisition.

Atomic force microscopy (AFM) measurements: The AFM measurements were conducted utilizing the NX20 AFM instrument from Park Systems. Surface topographical images were acquired in tapping mode, employing a silicon tip with a resonant frequency of 300 kHz and a spring constant of 26 N/m. The root mean square (RMS) roughness values were extracted from a 5μm x 5μm image.

1.16 Determination of electronic band levels using Photoemission yield spectroscopy (PES)

PES (AC-2, Riken-Keiki) measurements were conducted to determine the valence band maximum (VBM) of the 3D, 2D ($BA_2FAPb_2I_7$) templated 3D perovskite samples. The measurements were performed under ambient conditions, with the samples being illuminated by monochromatic ultraviolet (UV) light. The UV photons used had energy levels exceeding the ionization energy (IE) of the sample being measured. These photons caused the ionization of an electron to the vacuum level, which, in turn, ionized a gas molecule in proximity to the surface, as detected by the instrument. During the measurement, the energy of the photons ranged from 4.2 eV to 6.2 eV, and the number of generated photoelectrons was recorded for each energy level. This recorded value was corrected based on the intensity spectrum of the UV lamp used. For semiconductors, the number of photo-generated electrons near the VBM typically increases as the cube root of the energy. Therefore, the cube root of the corrected PYSA spectrum was plotted against the photon energy. The linear region of the plot above the onset was fitted to determine the VBM, which was identified at the crossing point between the linear fit and the background level. To calculate the conduction band minimum (CBM) relative to the vacuum level, the measured bandgap was subtracted from the ionization energy, resulting in the electron affinity (EA).

1.17 Characterization of solar cell devices

Solar cell performances: The performances of the solar cells were obtained by measuring the current-voltage (J-V) curves of each device illuminated by an ABB solar simulator from Newport (model 94011). The arc simulator modelled AM 1.5G irradiance of 100 mW/cm^2 whose intensity was calibrated using a NIST-certified Si solar cell (Newport 91150V, ISO 17025) and corrected by measuring the spectral mismatch between the solar spectrum, reference cell, and the spectral response of the PV device. We estimate a mismatch factor of 3%. The solar cells were measured with a Keithley 2401 instrument from 1.2 to 0 V and back, with a step size of 0.05 V and a dwell time of 0.1 s, after light soaking for 10 s. The defined active area was 3.14 mm^2.

External quantum efficiency: The external quantum efficiency (EQE) of the solar cell devices was collected by first illuminating each device with monochromatic light modulated at 2 kHz coming from a quartz-tungsten-halogen light source fed into a monochromator (SpectraPro HRS 300, Princeton instruments). The photocurrent response of the solar cells was measured by an SR865 lock-in amplifier. The light source spectrum response was calibrated using a calibrated silicon diode (FDS1010, Thorlabs).

Stability tests: For stability test measurements, the perovskite devices were encapsulated with a UV- curable epoxy (Poland Inc.) and a glass coverslip as a barrier layer in an argon-filled glove box. The devices were blown with the argon gun to remove any contaminants or dust particles just before encapsulation. All the devices were tested at the continuous maximum power point condition, under full-spectrum simulated AM 1.5G (100 mA cm^{-2} irradiance) in the air using an ABB solar simulator (94011A, Newport) – ISOS-L1 protocol. Each data point was collected after an interval of 15 min. The relative humidity was measured to be constant at 60 ± 5 %R_H.

1.18 Mechanism of 3D $FAPbI_3$ formation.

In our synthesis methodology, we dispersed selective 2D perovskite crystals ($BA_2FAPb_2I_7$) in a $FAPbI_3$ solution containing FAI:PbI_2 (1:1) dissolved in a DMF: DMSO solvent. Subsequently, we observed sub-micrometer-sized crystallites, referred to as "memory seeds," which retained their perovskite structure and acted as nucleation sites during film formation (Fig. S14) *(41)*. Upon spin coating, these memory seeds transferred their n-value to the solution-processed films which comprises of 2D perovskite ($BA_2FAPb_2I_7$) alongside the δ-phase of $FAPbI_3$ (**Fig. 2E, Step i**). During annealing, we propose that the transformation to bulk $FAPbI_3$ occurs through an intercalation process (**Fig. 2E, Step ii**). Ions such as FA^+, Pb^{2+}, and I^- permeate the lattice from the edges of the 2D-HaP crystal, diffusing along the interface between the perovskite layers. These ions fill voids in the corner-sharing PbI_6 structure, forming additional linkages and integrating with the $[Pb_nI_{3n+1}]$ lattice to form the 3D bulk $FAPbI_3$ pushing the bulky organic cations to the grain boundaries (**Fig. 2E, Step iii**). The observed templating effect is attributed to the delicate ionic interactions between the 2D inorganic octahedral sheets and the organic spacers, coupled with the lattice matching between the 2D perovskite ($BA_2FAPb_2I_7$) and the 3D $FAPbI_3$ lattice planes. Our results are consistent with the previous reports that observe the intercalation of precursor ions into the lattice to form higher layer thickness 2D-HaP *(44)*.

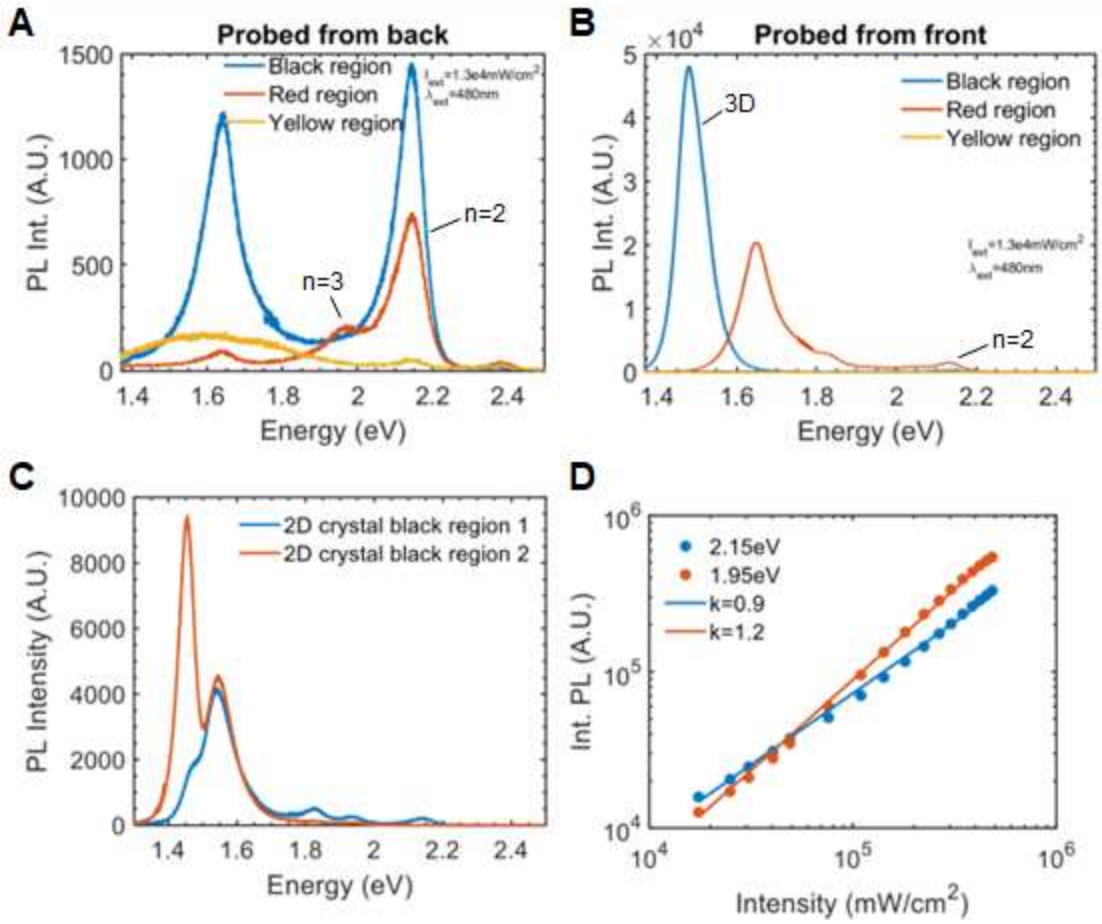

Fig. S1. Photoluminescence characterization of templated $FAPbI_3$ on $BA_2FAPb_2I_7$ single crystal. Photoluminescence of the 3 different regions on the templated $FAPbI_3$ drop-coating experiment from the back and the front (**A** and **B**, respectively). The red region is depicted as region (i) in **Figure 1D** and was the unexposed $FAPbI_3$ solution area of the $BA_2FAPb_2I_7$ single crystal. The black region is depicted as region (ii) in **Figure 1D** and was the edge of the $BA_2FAPb_2I_7$ single crystal that was in contact with the $FAPbI_3$ solution. The yellow region (region (iii) in **Figure 1D**) corresponds to the opposite edge of the sample where the $FAPbI_3$ sample is on glass. **C**. PL spectra of two different regions, one of which (region 1) is on top of the 2D crystal and the other (region 2) where there is no 2D crystal. **D.** Integrated PL peaks as a function of probe intensity for the n=2 and (hypothesized) n=3 excitonic peak (blue and red, respectively). The log-log linear fit constants are shown in the legend as the slope k.

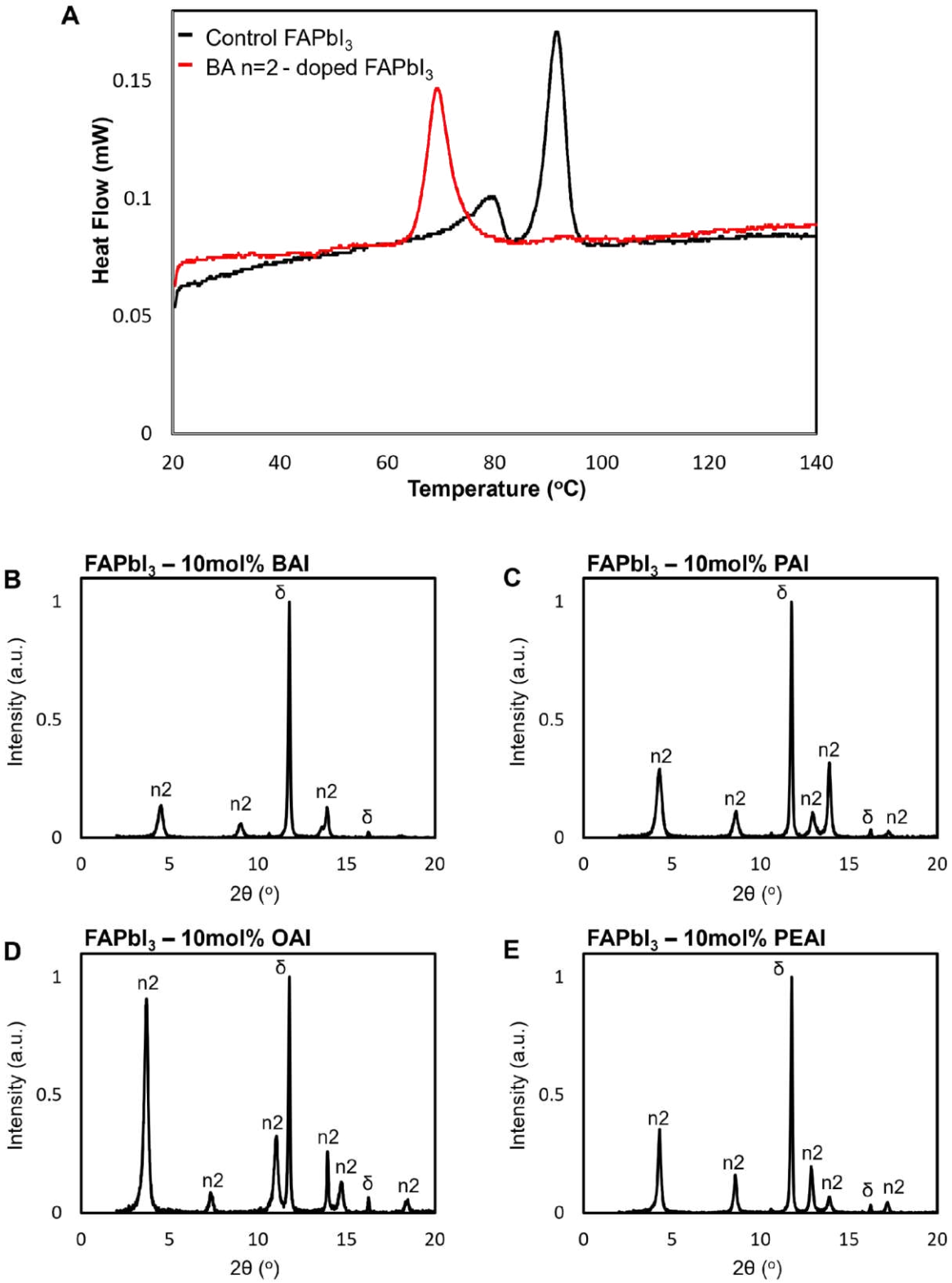

Fig. S2. Demonstrating the viability of 2D stabilization. A. Differential Scanning Calorimetry of a scraped $FAPbI_3$ film before annealing, with 2 mol% BA n=2 dopant (red) compared to without (black) showing $\delta \rightarrow \alpha$ conversion at lower temperature for 2D-doped $FAPbI_3$. **B – E.** 1D XRD of

films of spin-coated $FAPbI_3$ solution doped with 10mol% A' iodide salt, annealed for 5 min at 70°C. **B.** BAI, **C.** PAI, **D.** OAI, **E.** PEAI. In each case the A'I precipitates as phase-pure $A'_2FAPb_2I_7$.

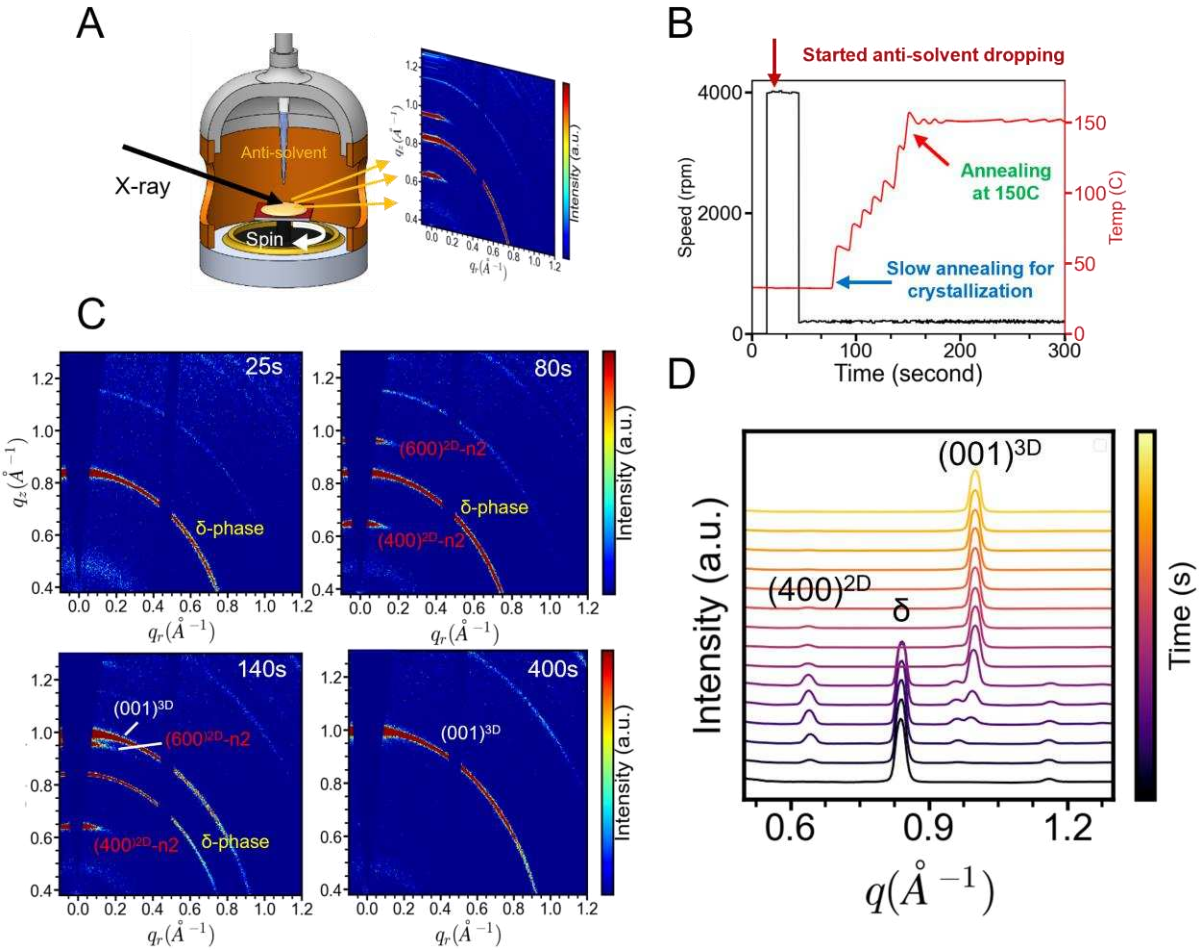

Fig. S3. In-situ structural probe during thin-film formation for 1.0 mol% $BA_2FAPb_2I_7$ doped $FAPbI_3$. A. Schematic of the in-situ wide-angle-x-ray-scattering experiment during film formation and an example of diffraction pattern obtain during measurement. **B.** An example of the experimental logs which track the spin-coating speed and temperature of the spin-coater hotplate during the measurement. The critical steps during the film-formation are noted on the plot such as the anti-solvent dropping, the time at which the annealing starts and the 150°C annealing. **C.** The corresponding WAXS diffraction patterns obtain during the measurement at critical times (noted on the top right). The Bragg diffraction planes for the 2D, α- and δ-phase are denoted on the plot in red, white, and yellow, respectively. **D.** The corresponding time evolution of the diffraction pattern during the thin-film formation.

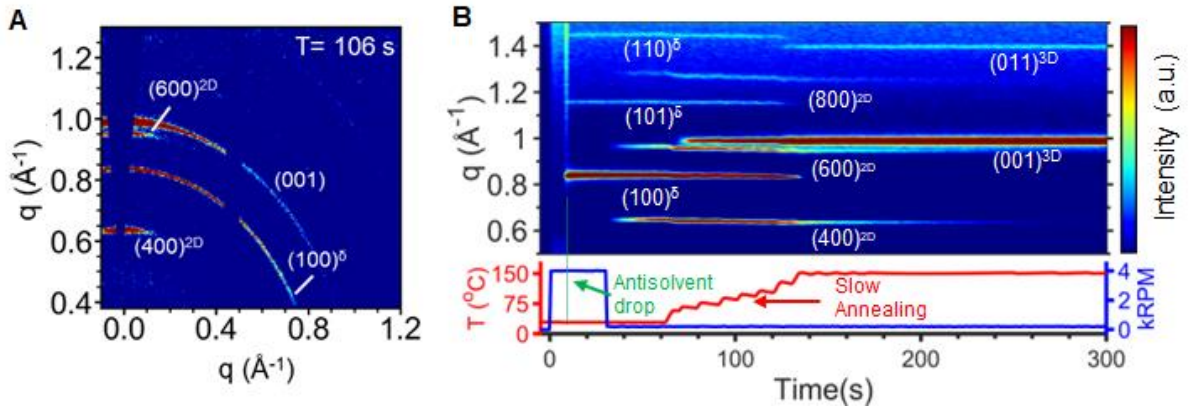

Fig. S4. A) WAXS pattern taken during thin-film formation showing the coexistence of δ-$FAPbI_3$, α-$FAPbI_3$, and $BA_2FAPb_2I_7$ diffraction peaks. **B)** Azimuthally integrated WAXS pattern over time during in-situ spin-coating of a $FAPbI_3$ precursor solution with 1.0 mol% BA n=2.

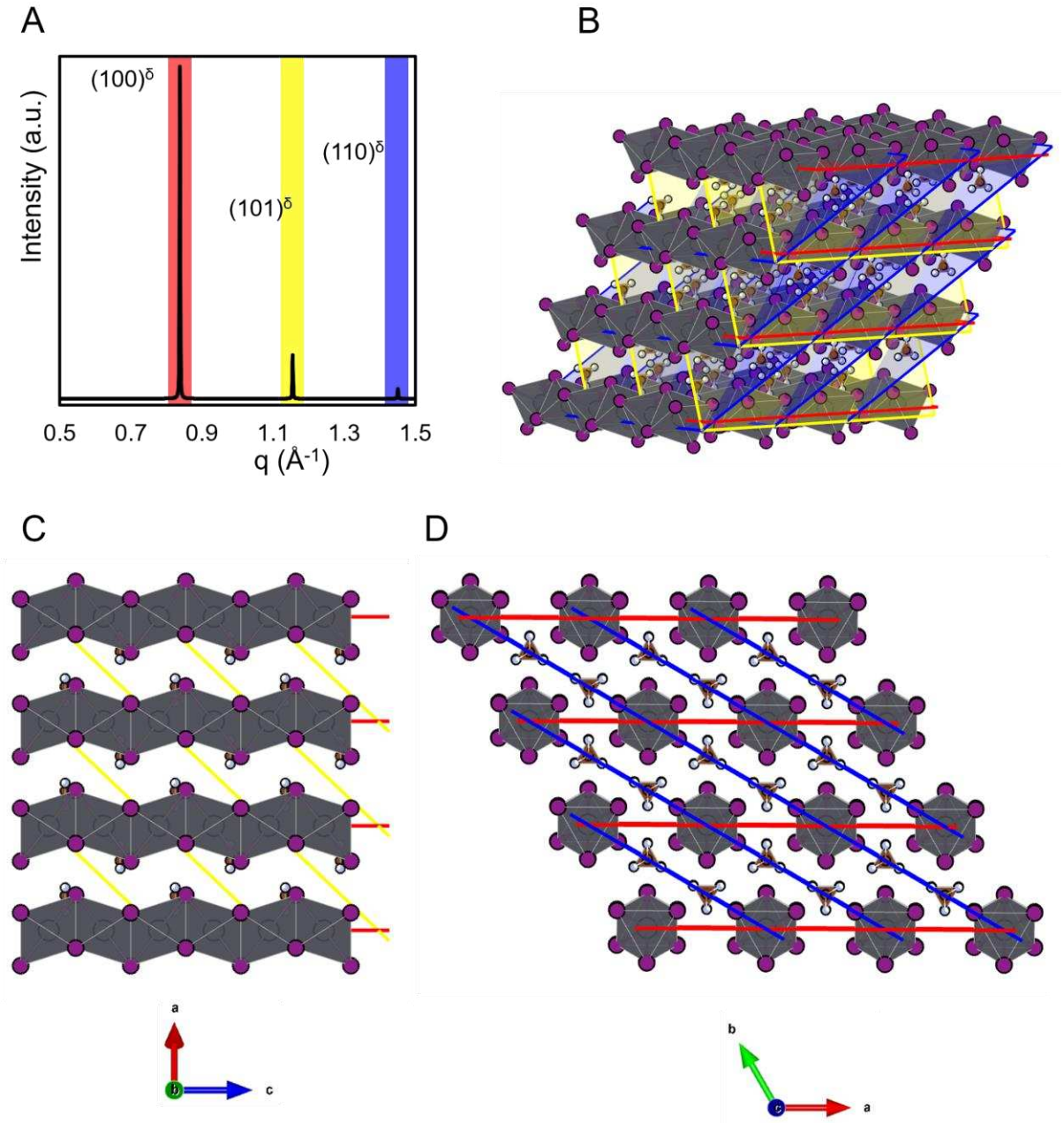

Fig. S5. Diffraction planes in the δ-FAPbI$_3$ structure. A. Simulated diffraction pattern for δ-FAPbI$_3$ showing the three lowest-angle diffraction peaks: (100) (red), (101) (yellow, and (110) (blue). **B.** The δ-FAPbI$_3$ structure with (100) (red), (101) (yellow, and (110) (blue) planes indicated. The structure is also shown along the b-axis (**C.**) and the c-axis (**D.**).

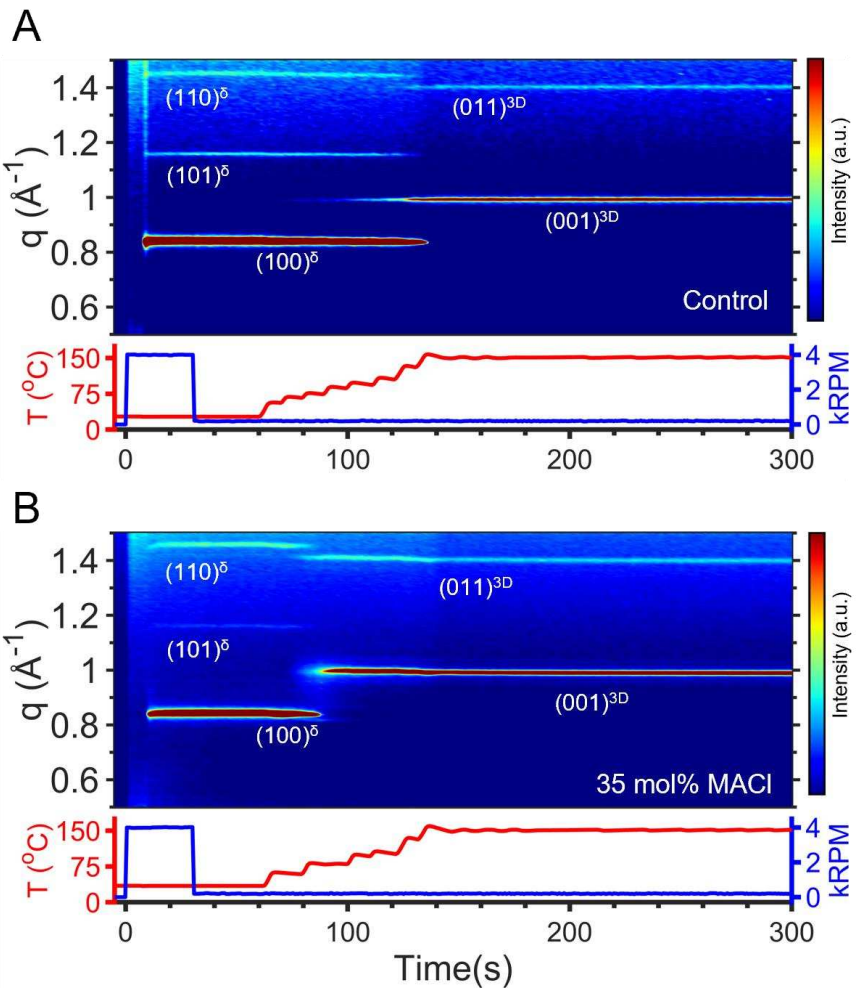

Fig. S6. **A-B.** Contour plot of the in-situ WAXS measurement for the fabrication of (**A.**) control-$FAPbI_3$ and (**B.**) $FAPbI_3$ doped with 35 mol% methylammonium chloride. Illustrated on the contour plots are Miller indices for the α (3D) and δ phases.

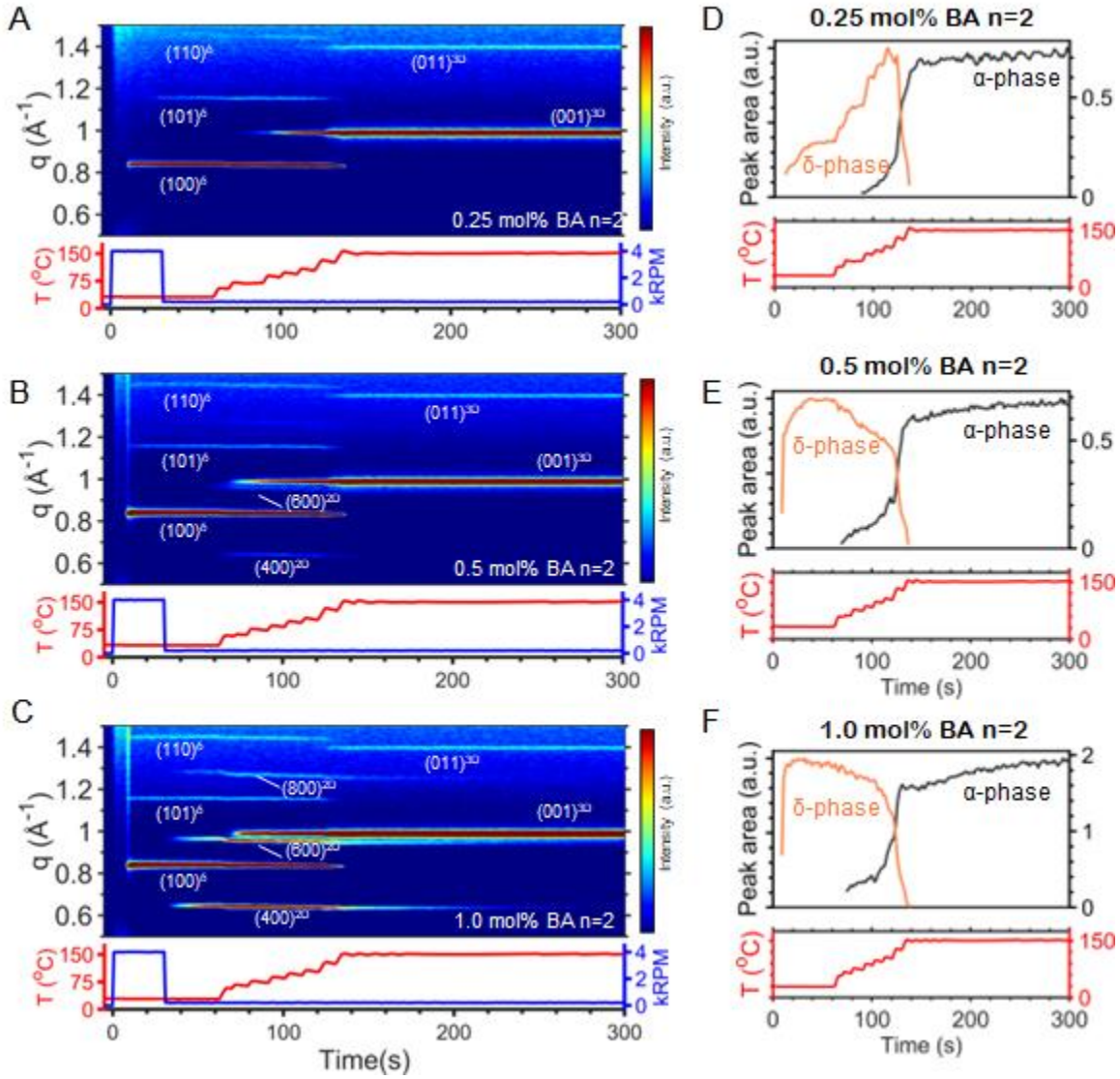

Fig. S7. Structural dynamics of $BA_2FAPb_2I_7$ -doped $FAPbI_3$ with different dopant concentrations during thin-film formation. A-C. Contour plot of the in-situ WAXS measurement for $FAPbI_3$ doped with 0.25 mol% (**A.**), 0.5 mol% (**B.**), and 1.0 mol% (**C.**) BA n=2 crystals. Illustrated on the contour plots are Miller indices for the α (3D), δ, and 2D phases. **D-F.** Integrated peak areas for the $(100)^{\delta}$ (orange) and $(001)^{3D}$ (black) peaks over time for 0.25 mol% (**D.**), 0.5 mol% (**E.**), and 1.0 mol% (**F.**) $BA_2FAPb_2I_7$ – doped $FAPbI_3$. The $(001)^{3D}$ peak area is normalized to the maximum of the $(100)^{\delta}$ peak area.

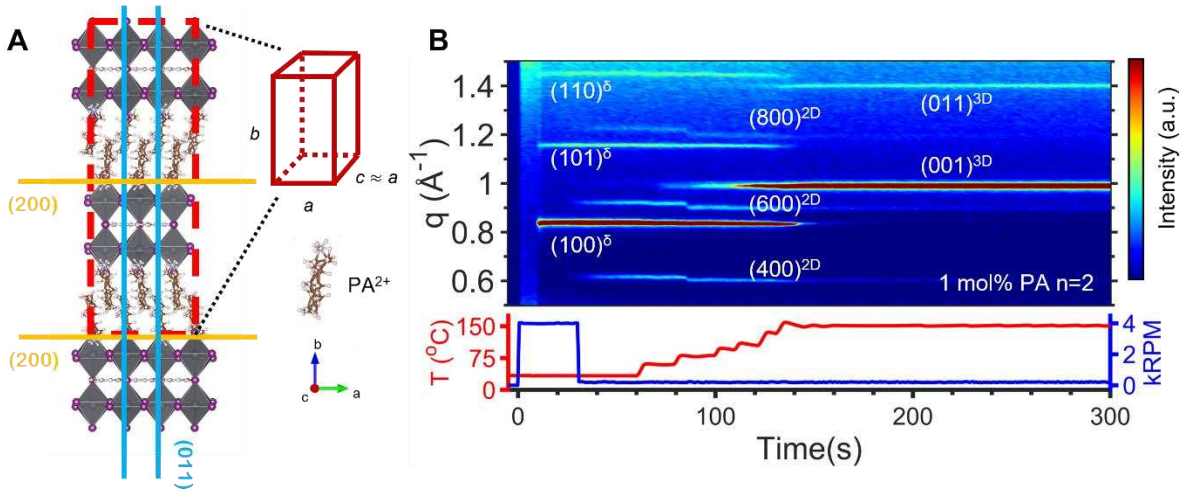

Fig. S8. Structural dynamics of $PA_2FAPb_2I_7$ doped $FAPbI_3$ during thin-film formation. A. Structure of the RP n =2 perovskites in the out-of-plane axis. The unit cell is indicated by the dashed line. The out-of-plane (002) **B.** Contour and parameter plot of the in-situ WAXS measurement for 1 mol% $PA_2FAPb_2I_7$ doped $FAPbI_3$. Illustrated on the contour plots are Miller indices for the α (3D), δ and 2D phases.

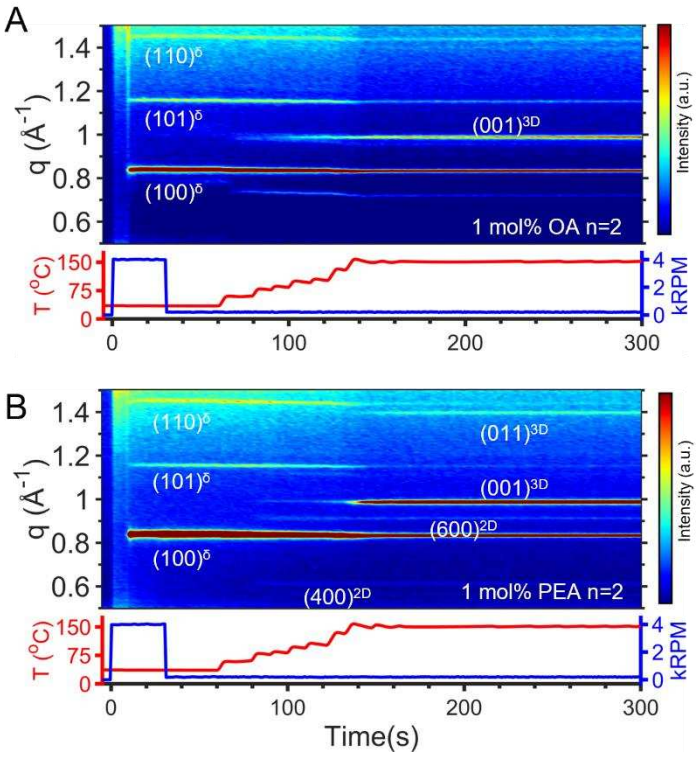

Fig. S9. Structural dynamics of $PEA_2FAPb_2I_7$ and $OA_2FAPb_2I_7$ doped $FAPbI_3$ crystals during thin-film formation. A-B. Contour plot of the in-situ WAXS measurement for 1 mol% PEA- (**A.**) and OA- (**B.**) based $FAPbI_3$ films. Illustrated on the contour plots are Miller indices for the α (3D) and δ phases.

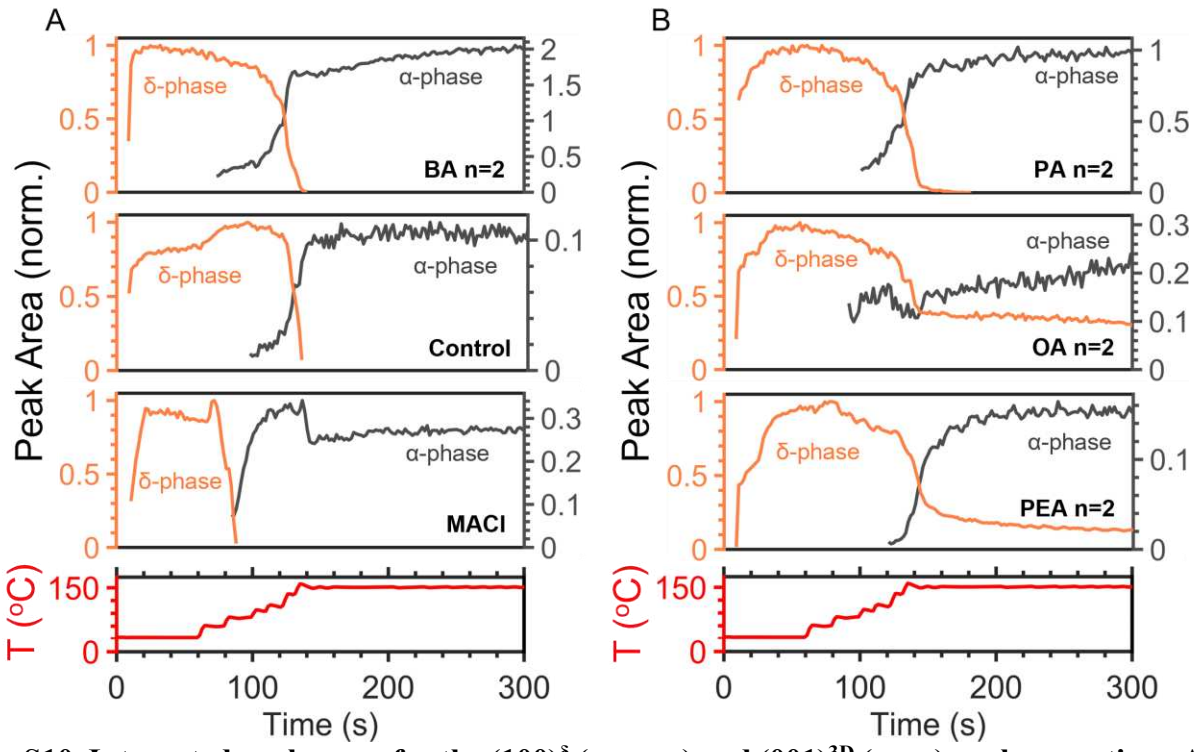

Fig. S10. Integrated peak areas for the $(100)^{\delta}$ (orange) and $(001)^{3D}$ (gray) peaks over time. A. 1 mol% $BA_2FAPb_2I_7$-doped $FAPbI_3$ (top), undoped $FAPbI_3$ (middle), and 35 mol% MACl-doped $FAPbI_3$ (bottom). **B.** 1 mol% $PA_2FAPb_2I_7$-doped $FAPbI_3$ (top), 1 mol% $OA_2FAPb_2I_7$-doped $FAPbI_3$ (middle), and 1 mol% $PEA_2FAPb_2I_7$-doped $FAPbI_3$ (bottom). The $(001)^{3D}$ peak area is normalized to the maximum of the $(100)^{\delta}$ peak area.

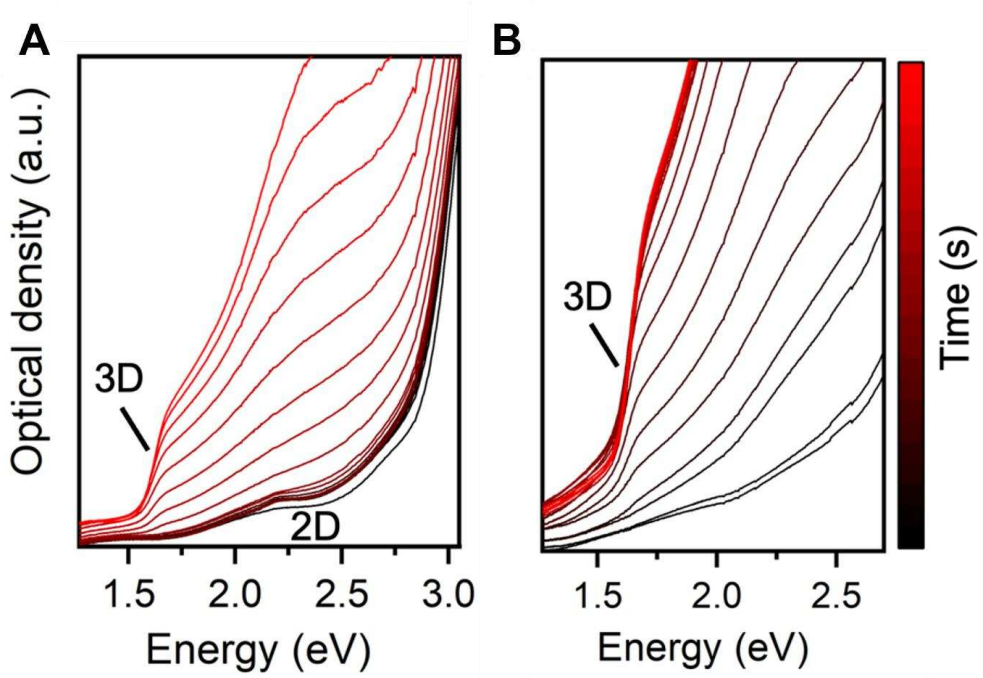

Fig. S11. In-situ optical absorption during thin-film annealing at 150 °C. Evolution of absorption pattern for the $BA_2FAPb_2I_7$ 2D doped $FAPbI_3$ (**A.**) and the control (**B.**) thin-films at 150°C. The gradient color represent time from 0s to 300s.

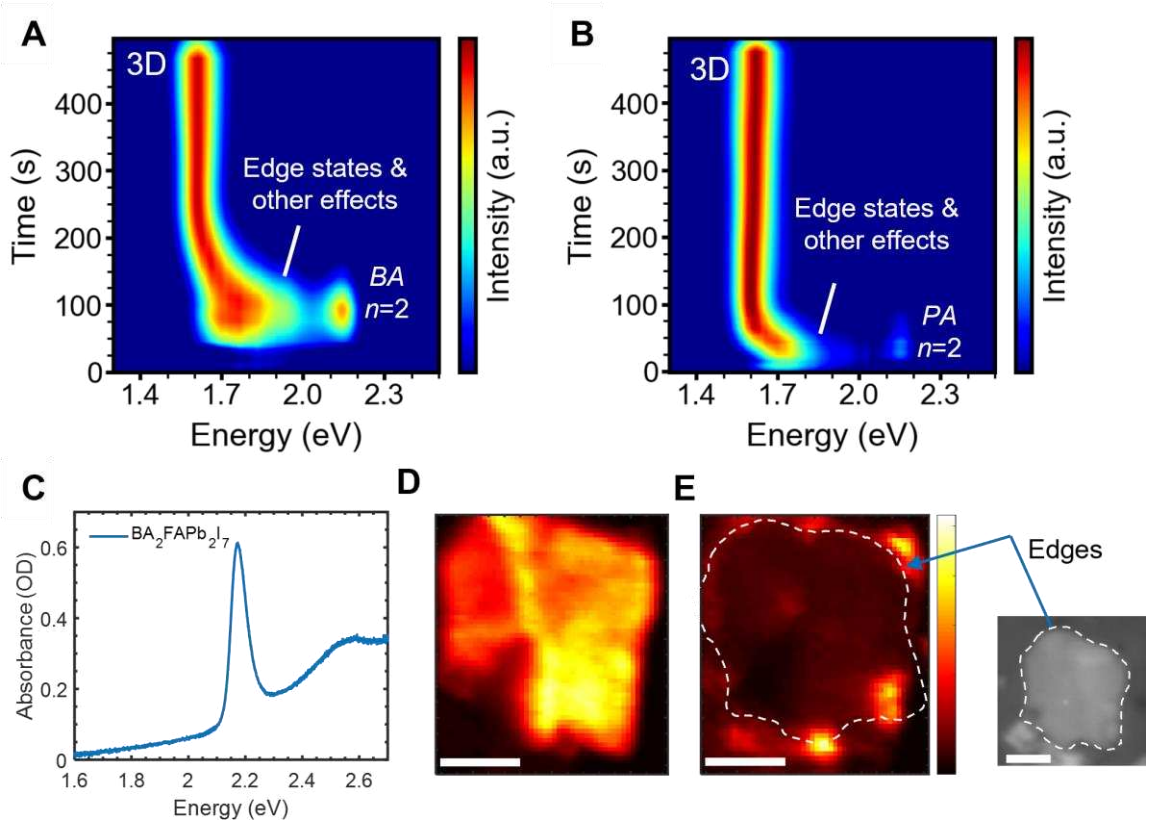

Fig. S12. Optical properties of 2D doped $FAPbI_3$ perovskite film and origins of low energy emission. A - B. In-situ photoluminescence measurement of the 0.5 mol% $BA_2FAPb_2I_7$ (**A.**) and $PA_2FAPb_2I_7$ (**B.**) doped $FAPbI_3$ during thin-film formation at 150°C. Denoted on the figure are the corresponding emission from different phases. The observed distribution in the bandgap from the n=2 2D perovskite to the $FAPbI_3$ perovskite observed in Fig. S12 (A-B) serves as a clear indication of the intercalation process leading to higher n and eventually 3D $FAPbI_3$ during the annealing process. Notably, pentylammonium (PA) exhibits lower rigidity (longer alkyl chain) compared to the butylammonium organic cation. This increased flexibility accelerates the intercalation process, resulting in a faster conversion to the 3D $FAPbI_3$ band gap within 100 seconds. Conversely, the butylammonium demonstrates a wider bandgap distribution and takes a longer time (200 seconds) to convert to the $FAPbI_3$ band gap. **C.** Optical absorption spectra of an exfoliated single crystal $BA_2FAPb_2I_7$ perovskite. **D. and E.** The corresponding photoluminescence intensity map probed at 2.14 eV (exciton ground state) (**D.**) and 1.81 eV (**E.**). Microscopic image showing the exfoliated perovskite on the right. Scale bar is 10 µm.

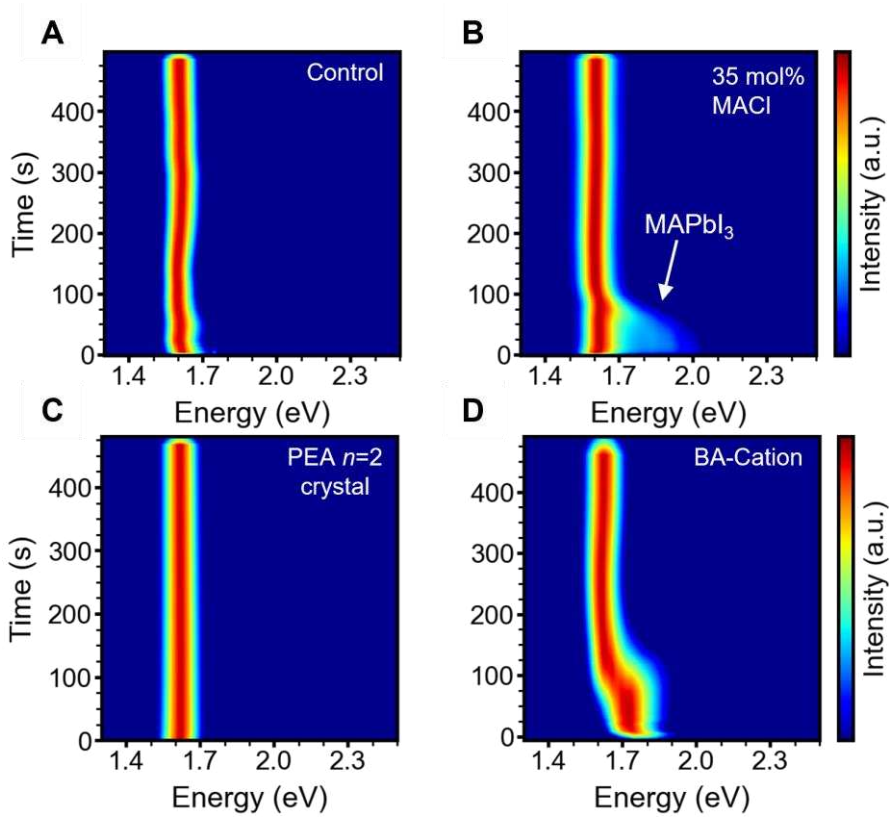

Fig. S13. In-situ photoluminescence spectra during thin-film annealing at 150°C. Heat-plots for time-dependent photoluminescence spectra of control (**A.**), MACl doped (**B.**), 1.0 mol% $PEA_2FAPb_2I_7$ (**C.**) and 1.0 mol% BAI doped (**D.**) $FAPbI_3$ films at 150°C. The emission peak from the $MAPbI_3$ 3D perovskite is labelled on subplot (**B.**)

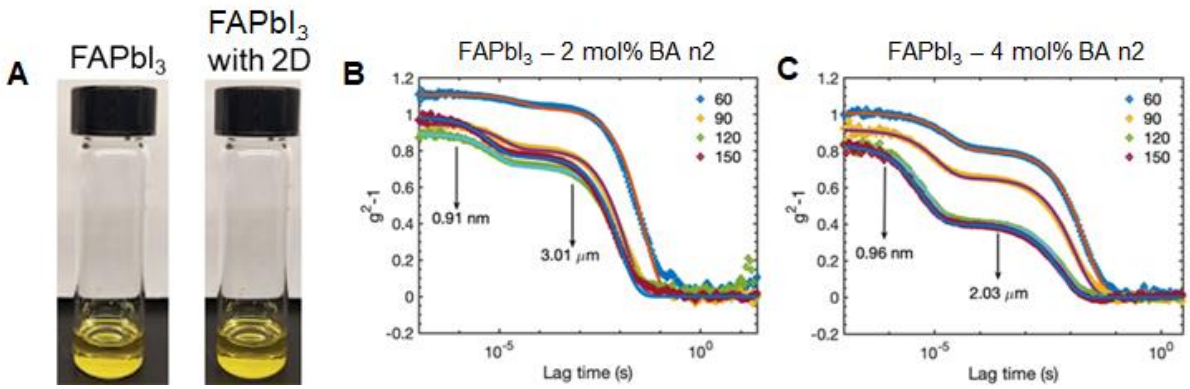

Fig. S14. A. Optical images of precursor solution of (left) pure $FAPbI_3$ and (right) $FAPbI_3$ with 2D seeds. **B, C.** Dynamic Light scattering measurement of different concentrations of $BA_2FAPb_2I_7$ dopants. Correlation function (g^2) versus lag time measured at several scattering angles overlayed with the corresponding fits to determine the particle size.

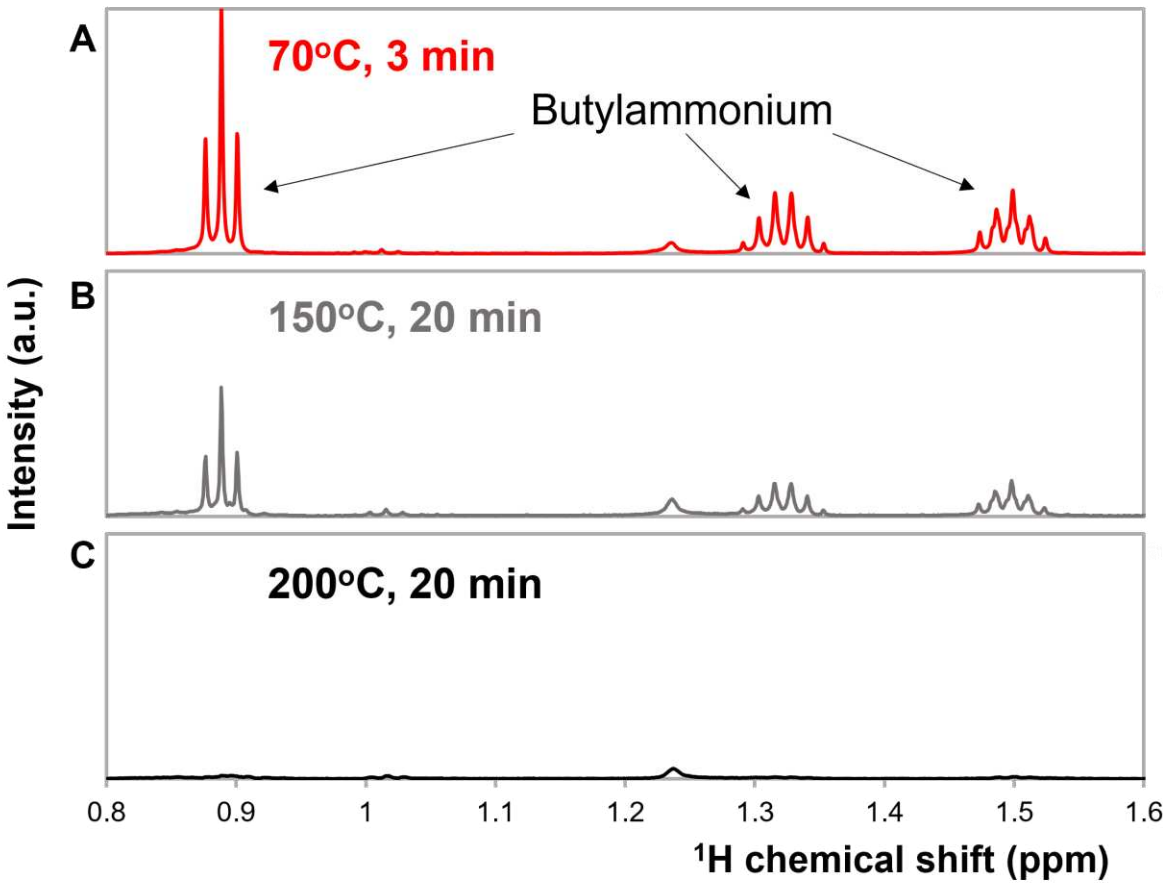

Fig. S15. Solution-state ^{1}H NMR spectra of 2D-stabilized $FAPbI_3$. NMR of $FAPbI_3$ – 5 mol% BA n=2 films annealed at (**A.**) 70°C for 3 min, (**B.**) 150°C for 20 min, and (**C.**) 200°C for 20 min. A higher BA n=2 concentration was employed to better resolve the butylammonium signal. Films were scraped with a blade and the resultant powder was dissolved in deuterated DMSO. Spectra normalized to the FA peaks (not shown). After annealing for 20 min at 150°C ~65% of the initial BA remains in the film. After 20 min at 200°C nearly all BA has left the film.

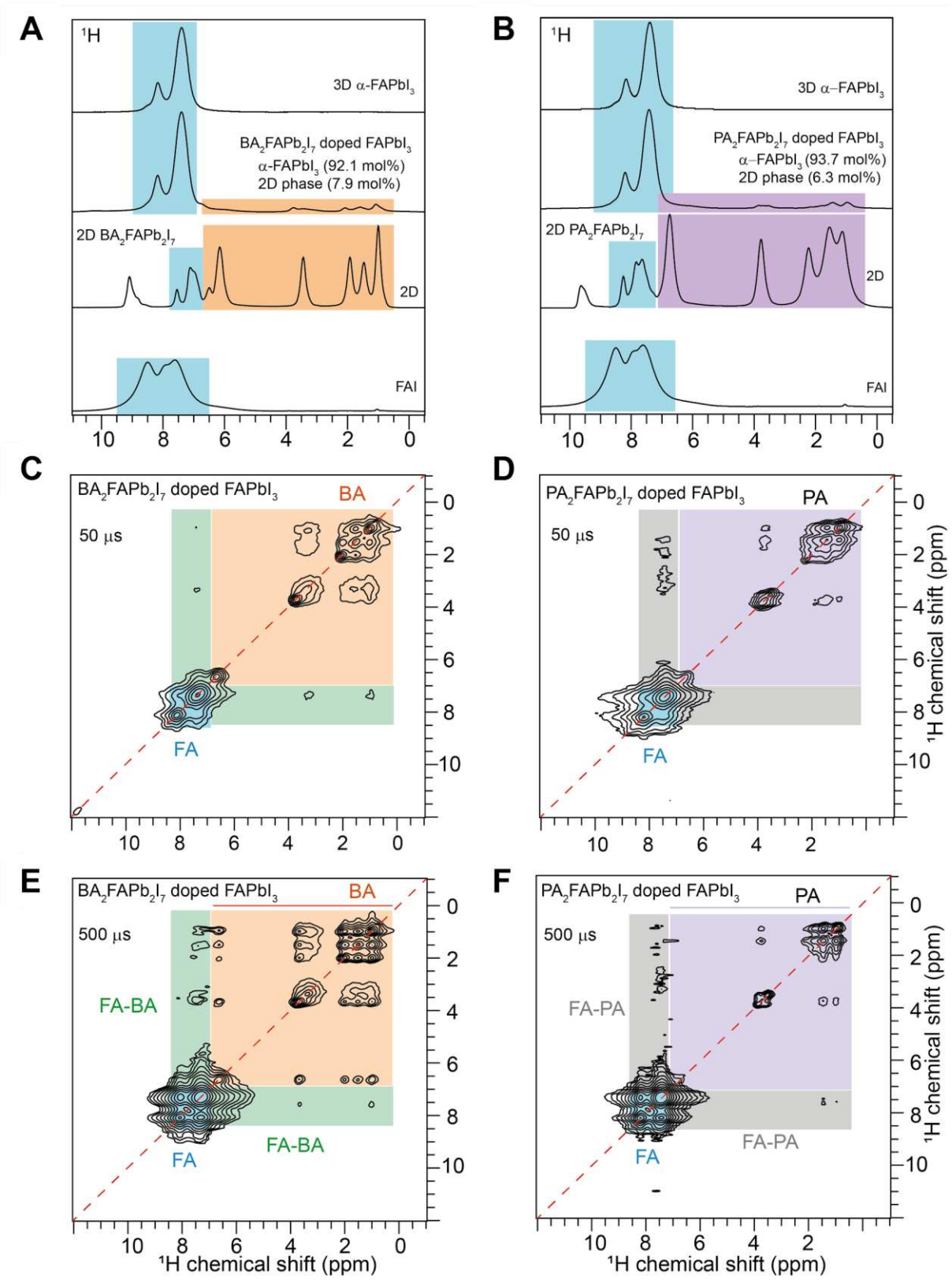

Fig. S16. Solid-state 1D 1H NMR spectra of 2D-stabilized FAPbI3. a-b. Comparison of 1 mol% $BA_2FAPb_2I_7$ and $PA_2FAPb_2I_7$ with stabilized $FAPbI_3$ after annealing films for 20 min at

150ºC in ambient air. **c-f.** 2D 1H-1H correlation NMR spectra of the 2D doped materials with coloured boxes in the insets indicating the peaks correspond to large (BA or PA) and small (FA) cations, and through-space interactions between them.

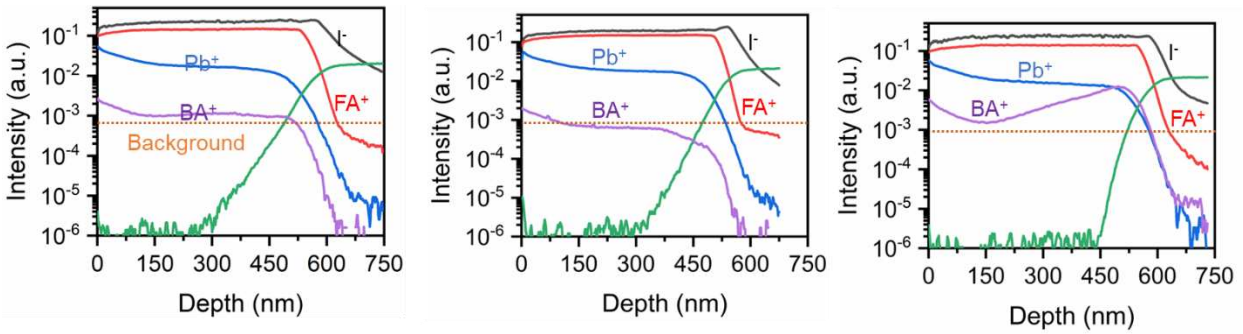

Fig. S17. ToF-SIMS of $FAPbI_3$ films. Left: 0 mol% $BA_2FAPb_2I_7$. Middle: 0.5 mol%. Right: 1.0 mol%.

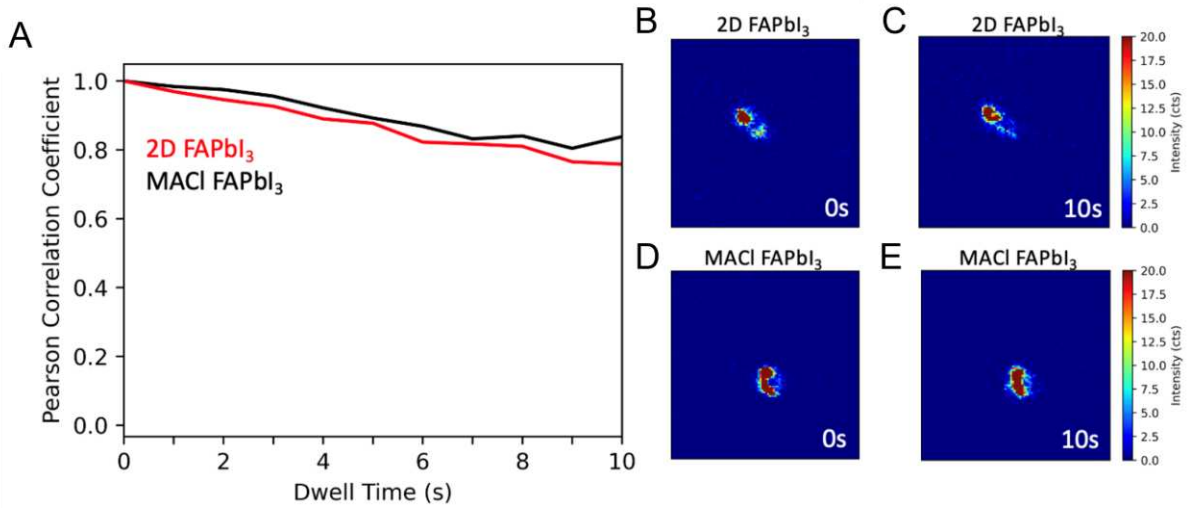

Fig. S18. X-ray stability over time with irradiation at a single point. A. Pearson correlation coefficient of the CCD image of the diffraction pattern with respect to the initial diffraction CCD image over 10 s of irradiation time. The substantial correlation over long times indicates X-ray stability much longer than the 100ms dwell time used for nanoprobe diffraction mapping. **B-C.** Diffraction CCD images from single point dwell of 2D $FAPbI_3$ at t=0 s (**B**) and t=10 s (**C**). **D-E.** Diffraction CCD images from single point dwell of MACl $FAPbI_3$ at t=0 s (**D**) and t=10 s (**E**).

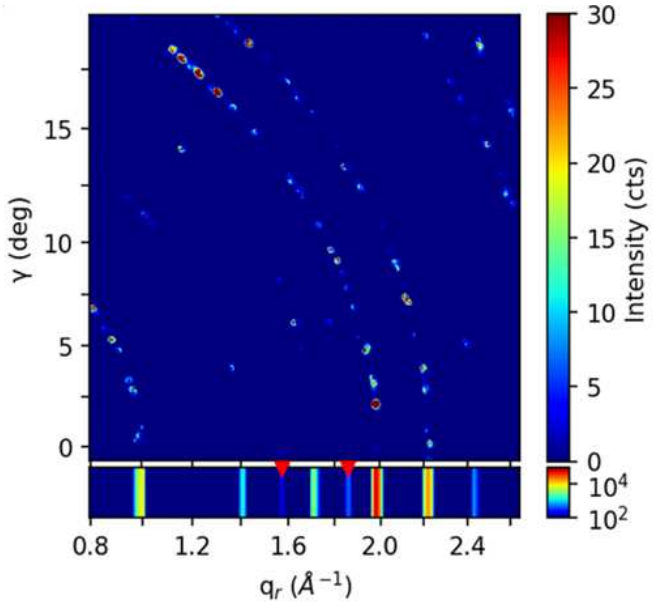

Fig. S19. Nanoscale structural properties. Top: Summed CCD image from a nano-diffraction mapping of a 2D-stabilized $FAPbI_3$ sample. Abscissa: q_r (A^{-1}), ordinate: azimuthal angle: γ (degrees). Bottom: azimuthally integrated diffraction pattern, plotted in log scale to make minority phases apparent. Red triangles denote indexed tetragonal peaks.

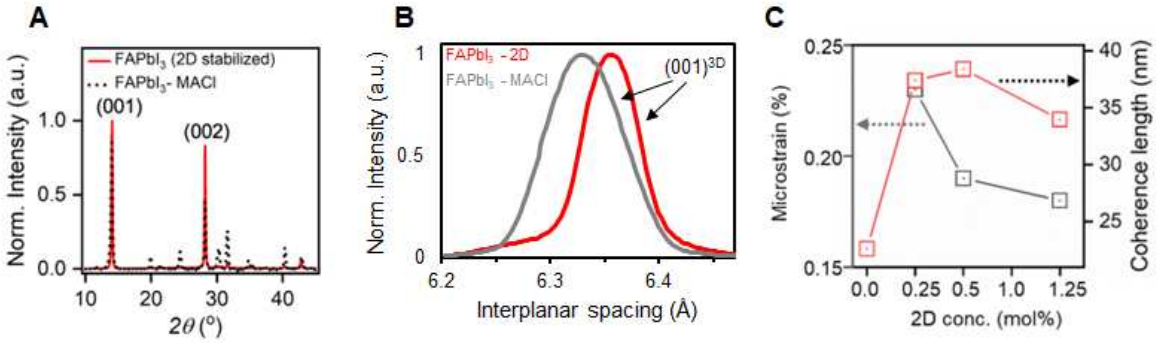

Fig. S20. Structural characterization of the $BA_2FAPb_2I_7$ and MACl doped $FAPbI_3$ thin film. **A.** Room temperature X-ray diffraction spectra of the $BA_2FAPb_2I_7$ and MACl doped $FAPbI_3$ thin film. **B.** Summed diffraction intensity as a function of interplanar spacing showing the $(001)^{3D}$ spacing for the $BA_2FAPb_2I_7$ and MACl doped $FAPbI_3$ thin film. **C.** Halder-Wagner analysis of the micro-strain and coherence length of various concentration of $BA_2FAPb_2I_7$ crystal doping.

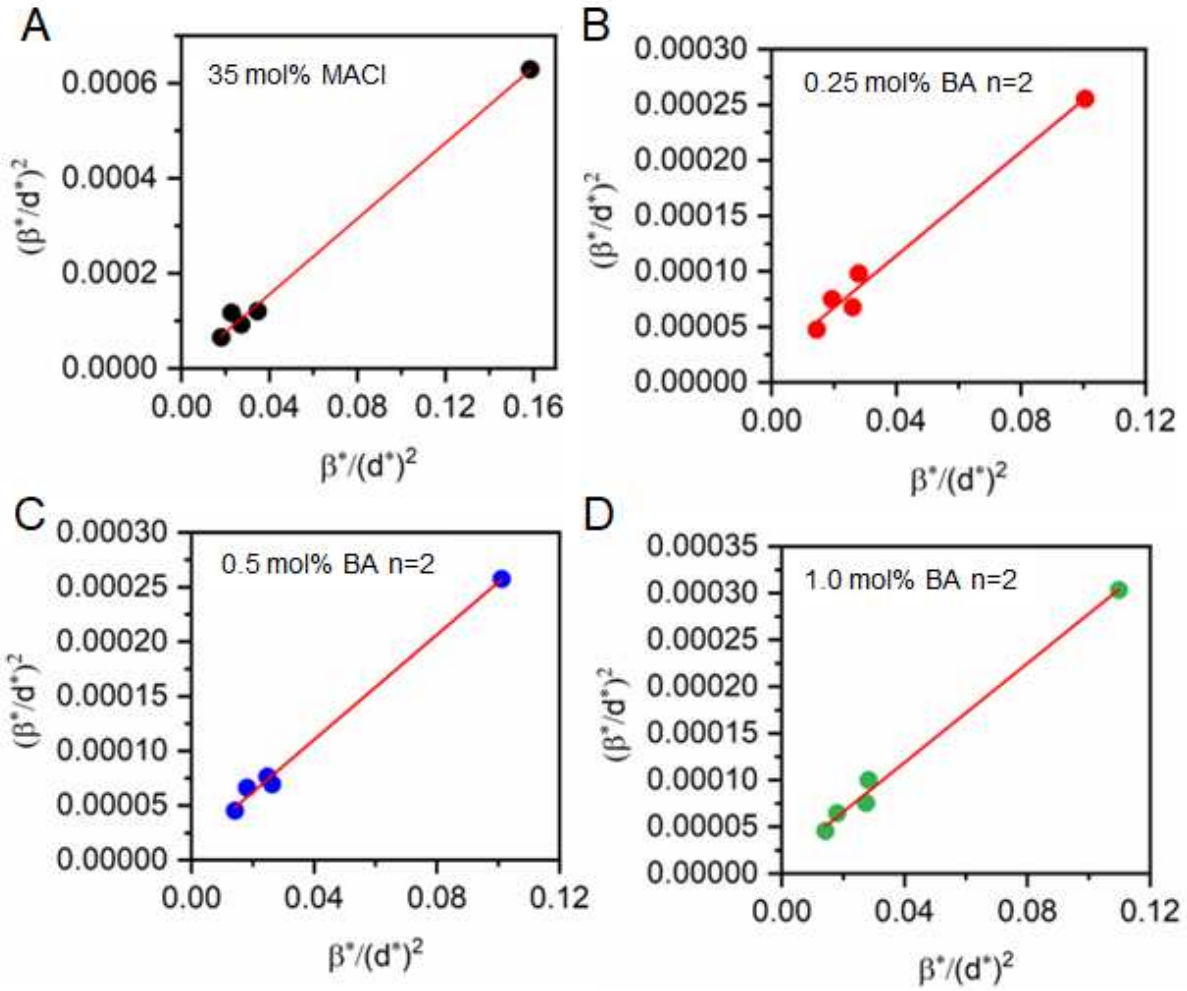

Fig. S21. Halder-Wagner plot for $FAPbI_3$ with various 2D dopant concentrations. A. 35 mol% MACl. **B.** 0.25 mol% BA n=2. **C.** 0.5 mol% BA n=2. **D.** 1.0 mol% BA n=2. The Halder-Wagner plot is used for extracting the strain ε and crystallite size D from XRD data using the equation $\left(\frac{\beta^*}{d^*}\right)^2 = \frac{K}{D} \cdot \frac{\beta^*}{(d^*)^2} + (2\varepsilon)^2$, where $\beta^* = \frac{\beta cos cos\, \theta}{\lambda}$ is the integral breadth of the reciprocal lattice point, $d^* = \frac{2 sin sin\, \theta}{\lambda}$ is the reciprocal lattice plane spacing, and K is the shape factor.

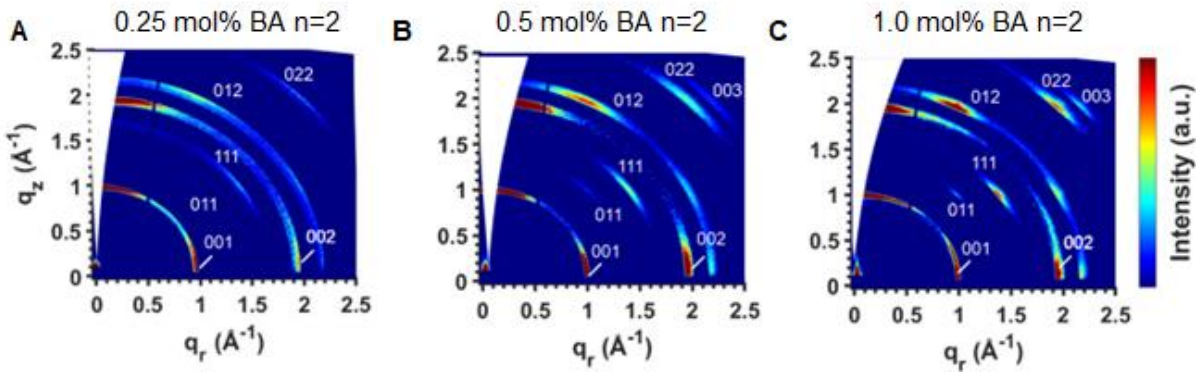

Fig. S22: Grazing Incidence Wide-Angle X-ray scattering patterns for various $BA_2FAPb_2I_7$ doping concentrations. **A.** 0.25 mol%. **B.** 0.5 mol%. **C.** 1.0 mol%.

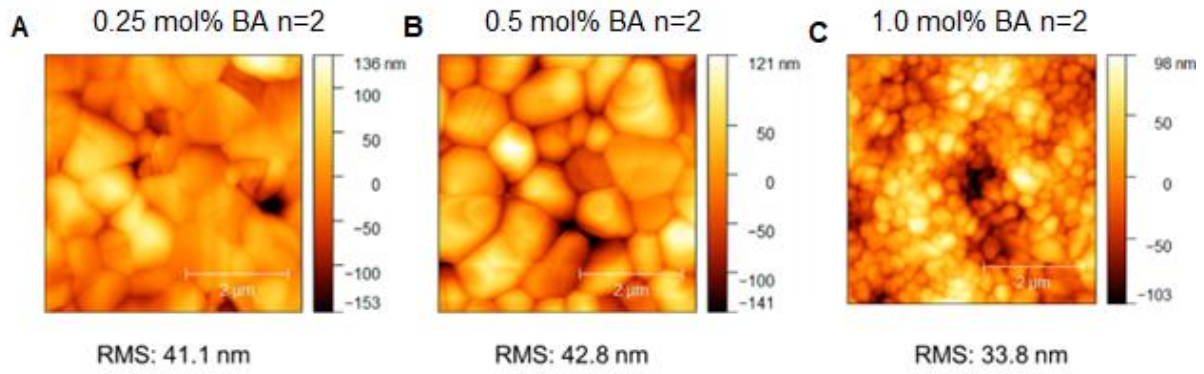

Fig. S23. Morphology of $FAPbI_3$ thin films. (a-c.) AFM images showing the variation in morphology of the $FAPbI_3$ thin film with different concentration of the 2D $BA_2FAPb_2I_7$ perovskite dopant with the extracted RMS roughness. **A.** 0.25 mol%. **B.** 0.5 mol%. **C.** 1.0 mol%.

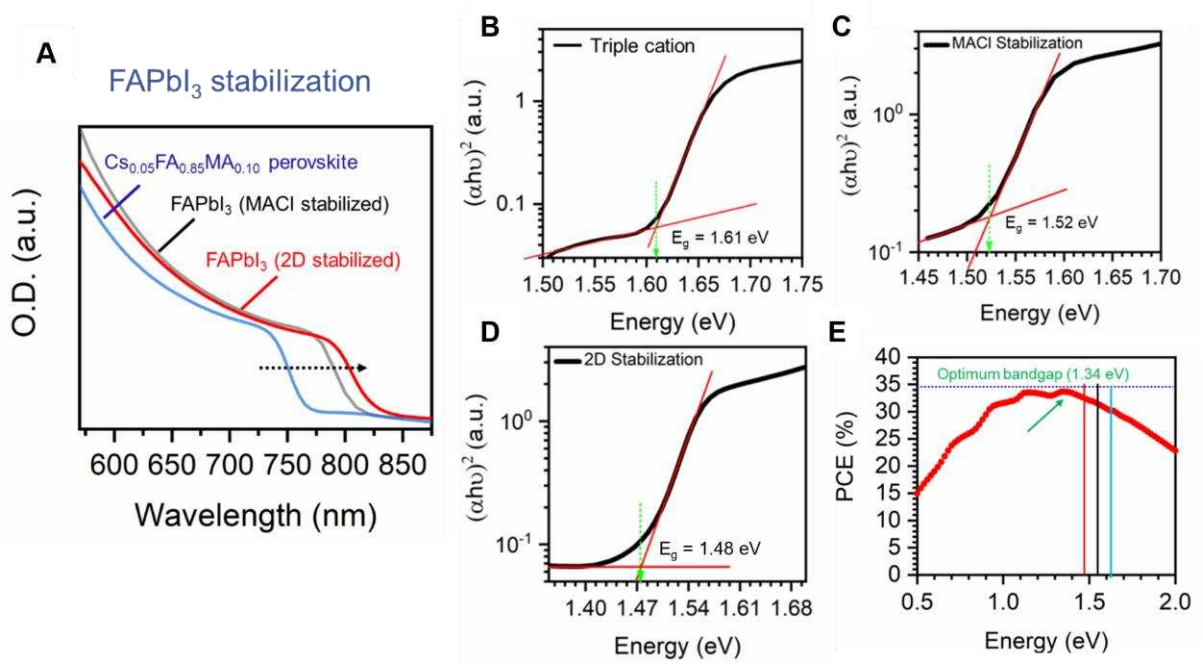

Fig. S24. Bandgaps of perovskite films. A. Absorption spectra of $Cs_{0.05}FA_{0.85}MA_{0.10}Pb(I_{0.9}Br_{0.1})_3$ (triple cation) films (blue), MACl-stabilized $FAPbI_3$ (black), and $BA_2FAPb_2I_7$-stabilized $FAPbI_3$ (red). **B-D.** Tauc plot of triple cation film (**B**), MACl-stabilized $FAPbI_3$ film (**C**), and 2D-stabilized film (**D**). **E.** Bandgaps of each film shown as vertical lines on the Shockley-Queisser limit curve.

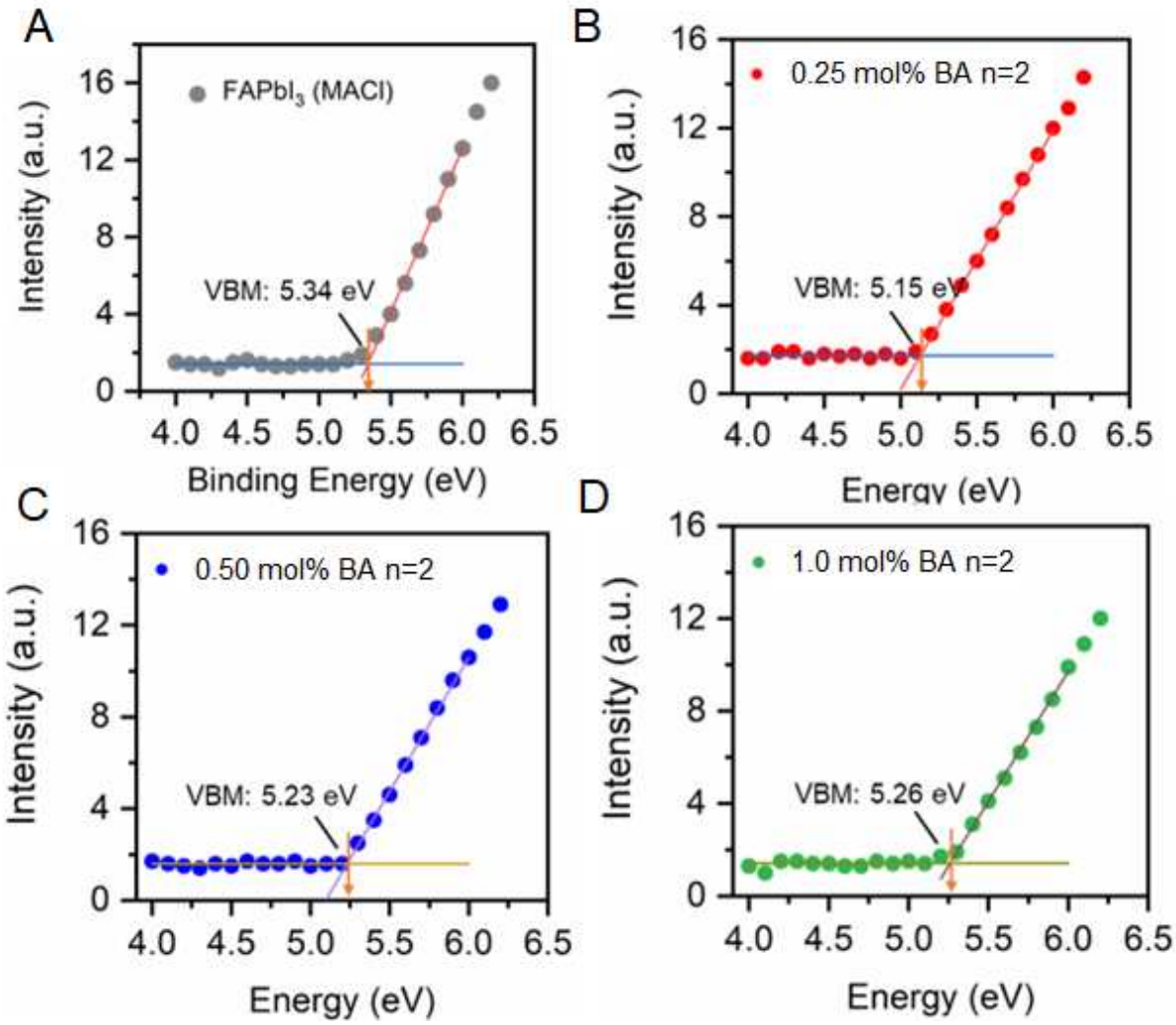

Fig. S25. PES Spectra. Plots showing the evolution of valence band maximum of the $FAPbI_3$ thin films with **A.** MACl doping, and **B-D.** different concentration of $BA_2FAPb_2I_7$ 2D perovskite. **B.** 0.25 mol%. **C.** 0.50 mol%. **D.** 1.0 mol%. The onset of signal indicates the position of the valence band maximum.

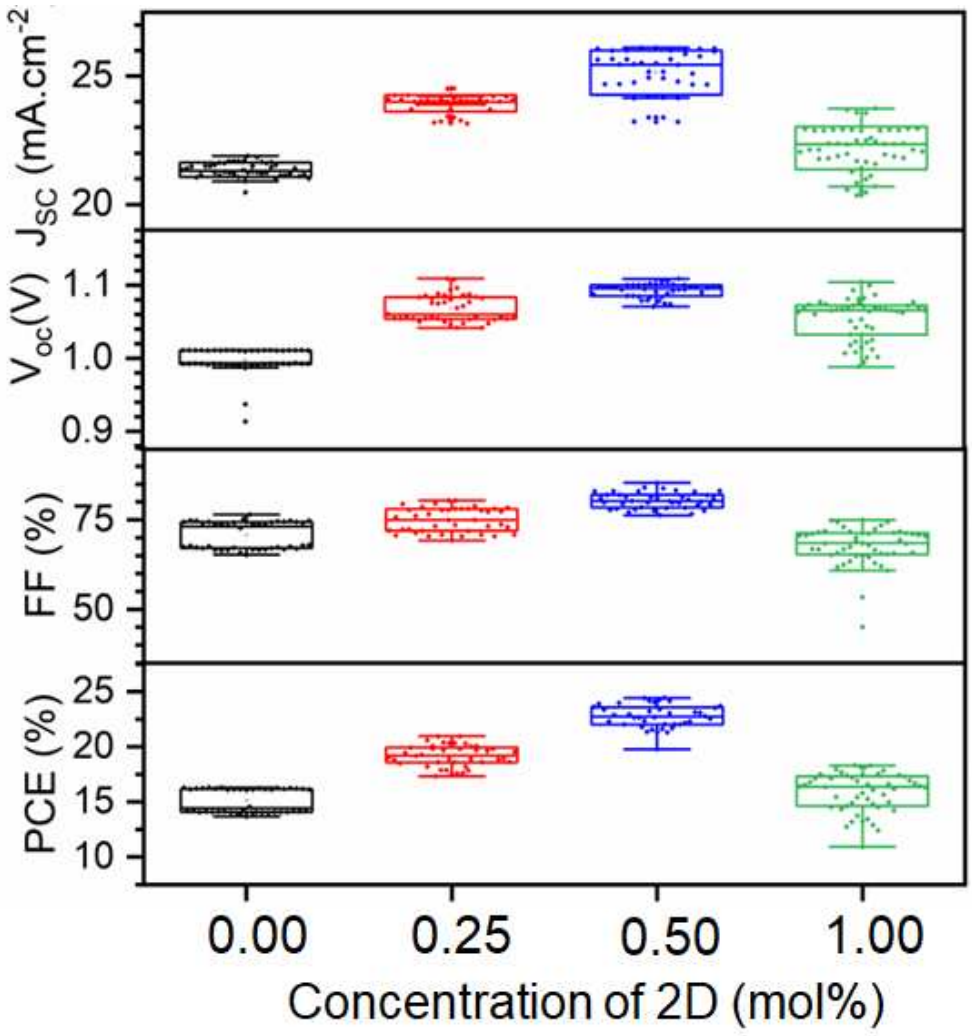

Fig. S26. Distribution of J-V parameters from $FAPbI_3$ devices with various molar doping concentrations of $BA_2FAPb_2I_7$.

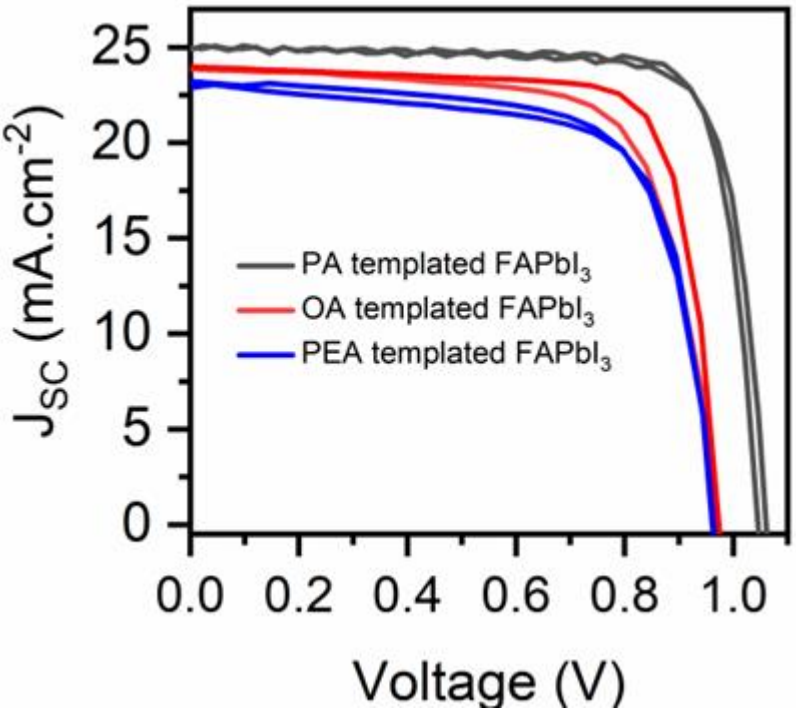

Fig. S27. Plot showing the J-V curve of the champion device fabricated with 0.5 mol% of different 2D perovskite stabilization of $FAPbI_3$.

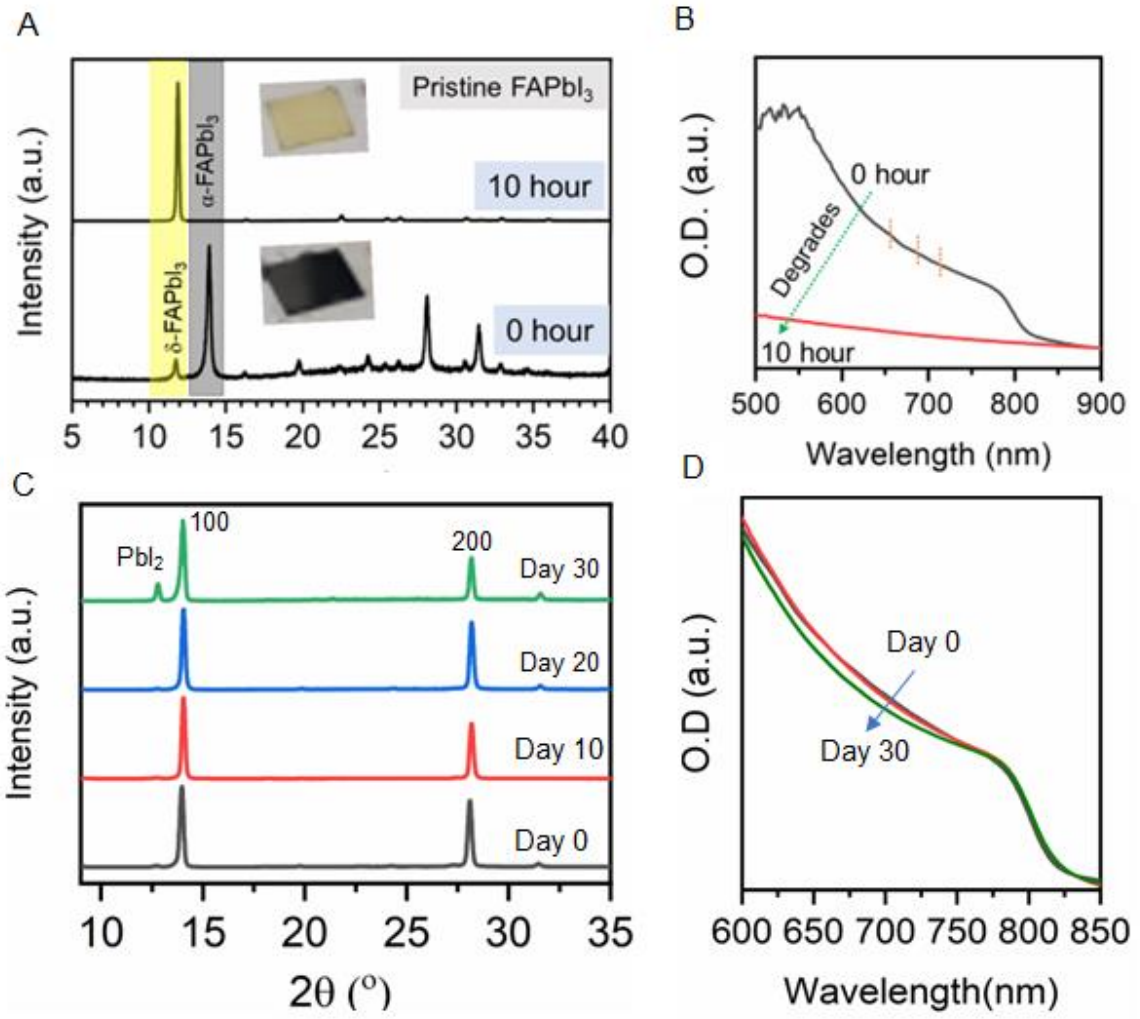

Fig. S28. Shelf life stability. A. 1D XRD and color images of undoped $FAPbI_3$ film. Bottom: pristine. Top: after 10 hr in ambient air. **B.** 1D XRD and color images of 0.5 mol% BA n=2-doped $FAPbI_3$ film. Bottom: pristine. Middle: after 10 days in ambient air. Top: after 30 days in ambient air. **C-D.** Optical absorption spectra for pristine and 10 hr degraded undoped $FAPbI_3$ film (**C**) and pristine, 10 days degraded, and 30 days degraded 0.5 mol% BA n=2-doped $FAPbI_3$ film (**D**).

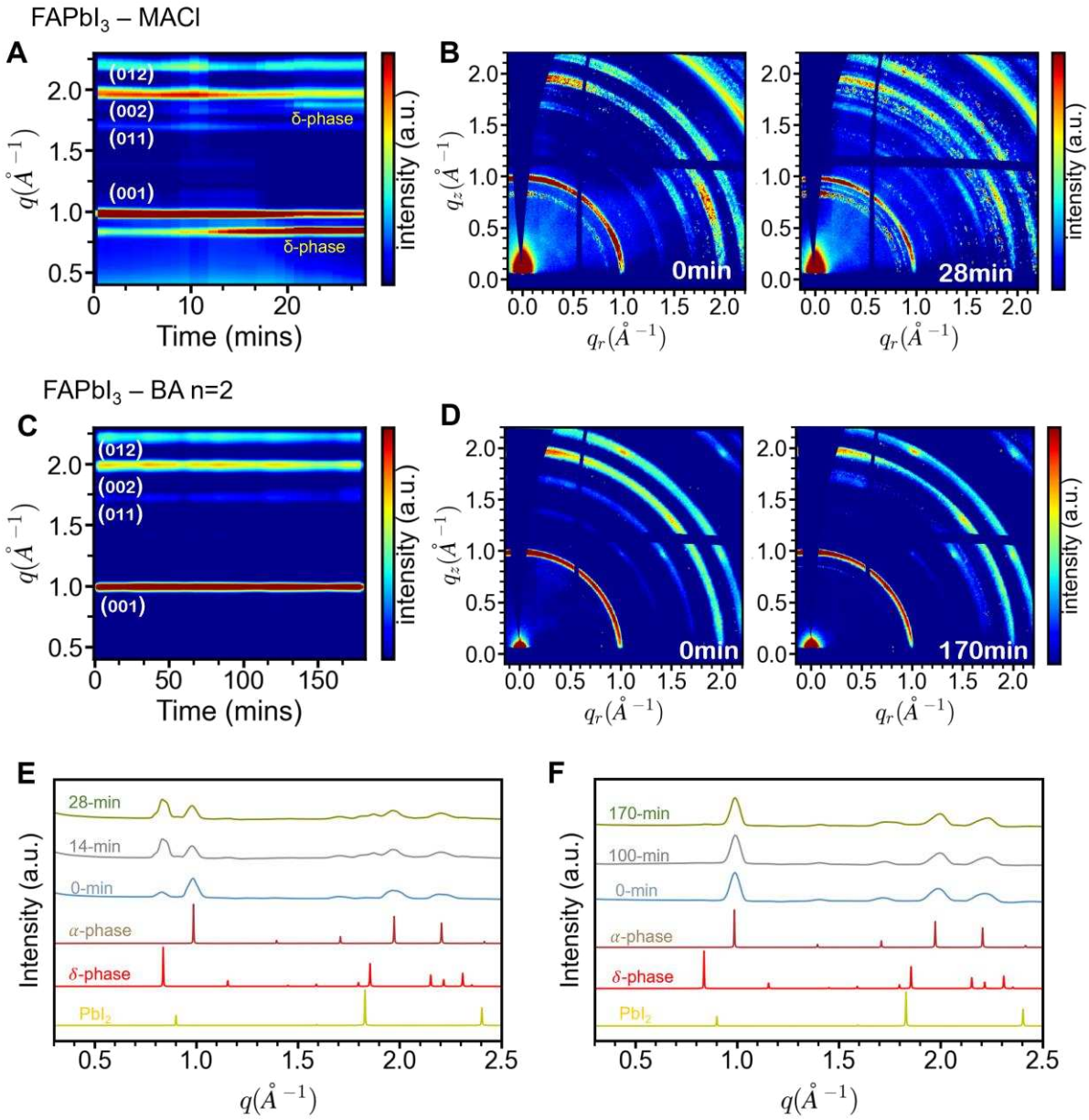

Fig. S29. In-situ WAXS of degrading MACl-doped $FAPbI_3$ and BA n=2-doped $FAPbI_3$ p-i-n devices at >90%RH, 1-sun illumination, and 65°C. Device architecture is as reported above, with a thinner (30nm) Au layer to allow the light and X-ray beam to penetrate. **A.** Azimuthally-integrated GIWAXS pattern over time for $FAPbI_3$-MACl device. **B.** GIWAXS pattern at 0 min (left) and 28 min (right) for the $FAPbI_3$-MACl device. **C.** Azimuthally-integrated GIWAXS pattern over time for the $FAPbI_3$-2D device. **D.** GIWAXS pattern at 0 min (left) and 170 min (right) for the $FAPbI_3$-2D device. **E.** Azimuthally-integrated GIWAXS pattern at 0 min, 14 min, and 28 min for $FAPbI_3$-MACl device, with α-$FAPbI_3$, δ-$FAPbI_3$, and PbI_2 diffraction peaks also shown. **F.** Azimuthally-integrated GIWAXS pattern at 0 min, 100 min, and 170 min for $FAPbI_3$-2D device, with α-$FAPbI_3$, δ-$FAPbI_3$, and PbI_2 diffraction peaks also shown.